



Influence of surface preparation and polymer backing properties on the quasi-static and impact response of ceramic faced 1D armour systems

Tom Commins^{*}, Aaron Graham, Clive R Siviour

Department of Engineering Science, Parks Road, Oxford, OX1 3PJ, United Kingdom

ARTICLE INFO

Keywords:

Armour
Composite
Impact
Quasi-static
Beam bend
Polymer
Prony series
Polyurethane
Time-temperature superposition
DIC
Fea
TSL

ABSTRACT

Ballistic impact is a highly complex environment, the understanding of which is compounded by the advanced materials used for ceramic-polymer composite armours. In this study, the influence of surface preparation and polymer backing properties on the energy absorptive capabilities and ballistic performance of simplified model armours was approached via a methodical investigation using simplified materials and geometries. Quasi-1D (beam) specimens consisting of polyurethane-backed alumina were loaded under three-point bend quasi-statically and at impact speeds. The specimen geometries allowed for the fracture pathways to be observed. To produce the specimens, two polyurethanes with different glass transition temperatures were cured onto alumina strips, eliminating the requirement for a dedicated adhesive and thus simplifying the interfacial dynamics. Further modifications were made by applying a primer surface treatment, by using unbonded polyurethane and adhered polyurethane, and by replacing the polyurethane with glass-reinforced polycarbonate. The beam specimens were loaded quasi-statically at 0.05 mm s^{-1} at ambient and sub-ambient temperatures, and at $50\text{--}300 \text{ m s}^{-1}$ at ambient temperatures. The quasi-static specimens were found to fail by one of two failure modes with approximately a 3x energy absorption difference; the failure was highly dependant upon the interface and polymer characteristics. Under impact, a significant proportion of the energy absorption was provided by the kinetic energy of the fragments. Although, the polymer backing and interfacial properties were found to influence fracture paths during loading. FEA simulations were used to model the behaviours using characterisation data from a previous study; these were found to predict the experimental response well.

1. Introduction

Composite structures are often used for defence against high energy projectiles. Personnel armours typically consist of a hard ceramic strike face and a more ductile polymer backing [1–3]. When the composite armours are impacted, stress waves propagate through the ceramic material. On reaching the interface between the strike and backing plates, due to the impedance mismatch, reflected and transmitted waves are generated [4]. These are highly dependant upon the interface between the ceramic and polymer and significantly influences the overall performance of the armour [5–11]; however, these processes are not well understood and conflicting results are not uncommon in the literature. Furthermore, interfaces within the two base materials can heavily affect the overall armour response. For example, Yadav et al. found that for monolithic ceramic armours, separating the ceramic into 3 layers showed an increase in performance, whilst an increase to 6 layers reduced it [12]; Akella reported that increasing the number of layers can

weaken performance against a single impact, but improves the multi-hit capacity of the armour [13]. It has been suggested that in fact that there are 30 – 150 layers within a typical composite armour, including internal surfaces, air gaps and inter-ply interfaces within the polymer, which is often manufactured from bonded fibres of ultra-high molecular weight polyethylene (UHMWPE) [14]; however, given the high speed of stress waves (c. $10 \text{ mm}/\mu\text{s}$ in ceramic, or $1\text{--}2 \text{ mm}/\mu\text{s}$ across the polymer) the equilibrium time for stress waves within these layers will be very short.

The literature, therefore, emphasises the inherent complexity present in ballistics research. Hence, a study involving simplified materials, bonding and geometry can give insights into the properties that would otherwise be difficult to obtain. In the study reported in this paper, simple homogenous materials were used and the requirement for a layer of adhesive at the interface was removed entirely to simplify the ceramic-polymer interaction. Quasi-1D (beam) specimens consisting of alumina backed with a polyurethane that was directly cured onto the

^{*} Corresponding author.

E-mail address: Thomas.Commins@magd.ox.ac.uk (T. Commins).

<https://doi.org/10.1016/j.ijimpeng.2023.104708>

Received 25 January 2023; Received in revised form 18 May 2023; Accepted 15 June 2023

Available online 23 June 2023

0734-743X/Crown Copyright © 2023 Published by Elsevier Ltd.

(<http://creativecommons.org/licenses/by/4.0/>).

This is an open access article under the CC BY license

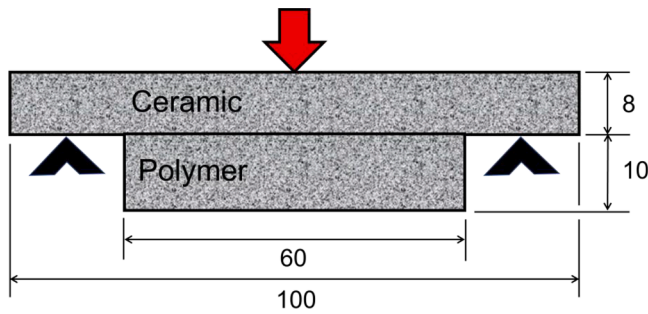


Fig. 1. Beam bend specimen schematic. All dimensions are in mm and specimens were 5 mm thick. The red arrow denotes the applied force.

Table 1
Quasi-static specimen type and environmental testing conditions.

Specimen Type	Backing	Bonding Condition	Test Temperature (°C)
1	None	–	
2	Task 3	Direct Curing – Primer and non-primer pre-treatment	20 and -49
3	Task 11	Direct Curing – Primer and non-primer pre-treatment	20, -36 and -49

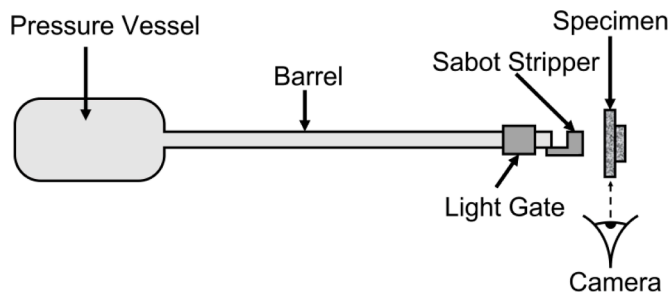


Fig. 2. Schematic of the gas gun used to investigate the impact behaviour of specimens under beam bend.

rear alumina face were loaded under quasi-static and ballistic loading. Due to the approximate plane stress nature of this geometry, the fracture pattern of the material could be observed on the material surface. Further, FEA simulations were conducted using previously determined interfacial properties to predict the quasi-static and ballistic behaviour.

Within this study, two polyurethanes with different glass transition temperatures were investigated: one above (55 °C), and one just below (15 °C), room temperature. This allows an investigation into stiffness and strain rate sensitivity: there is a rapid change in stiffness as the polymer passes through its glass transition. This change in stiffness arises from the ability, or lack thereof, of the polymer chains to move in response to an applied load; see, e.g., [15] for a detailed description. The position of the glass transition is influential because polymers loaded under impact can undergo a deformation rate-induced glass transition in which the polymer behaviour moves from rubbery to glassy, which significantly changes the energy dissipation characteristics [16–18]. There is also an opportunity to compare the rate and temperature dependence of the material behaviour to obtain a fuller picture of the nature of the armour response: separating structural from material changes. The use of chemically similar polymers helps make this comparison by reducing changes resulting from chemical interactions at the interface, which have been shown to strongly influence ballistic performance [10,11]. Further comparisons were drawn between these two polyurethanes using the presence or absence of a primer surface pre-treatment before adhesion. Additionally, the response of the model

armours was compared against glass filled polycarbonate, which is significantly stiffer than polyurethane.

2. Materials and specimen preparation

2.1. Materials

Polymer backed ceramics were manufactured using Sintox™ FF Alumina plates with a typical Al_2O_3 content of 95%, sourced from Morgan Ceramics [19]. For the polymer, two polyurethanes were obtained from Bentley Advanced materials [20] these are commercially known as ‘Task 3’ and ‘Task 11’, where Task 3 has a glass transition around 55 °C, and Task 11 around 15 °C (see Appendix). A detailed characterisation of the polymer is given in [21], and relevant properties are described in Section 5. No adhesive was used to bond the polymers; the baseline materials were allowed to cure in direct contact with the ceramic to form a bond, thus simplifying the interfacial dynamics. Further specimens were produced using a primer, Sika 206 G + P, to modify the interface properties.

Additional investigations were conducted using polymer backings consisting of 30% glass-fibre reinforced polycarbonate sourced from Ensinger [22], with a reported glass transition temperature of 147 °C. Dynamic mechanical analysis (DMA) experiments were performed (see Appendix), which show that this polymer has a modulus of around 3 GPa at room temperature and is relatively rate insensitive, with no significant transitions over the rates and temperatures of interest. To adhere this polymer to the alumina beams, Dowsil 6–1104 was used.

2.2. Specimen preparation

The baseline specimens consisted of thin alumina strips with the polyurethanes cured directly in contact with the rear face of the ceramic, Fig. 1. To produce these specimens, alumina strips of dimension $100 \times 8 \times 5$ mm were cut using a diamond saw from a 100 mm square plate. Before bonding the polymer, the surface was thoroughly cleaned using isopropyl alcohol, then water, and left to air dry. To create interfacial variation, for half of the specimens a thin layer of primer was applied to the ceramic surface using a lint free cosmetic sponge.

The polyurethanes used in this project were acquired as 2-part polymers and were degassed before and after mixing and once more when poured onto the ceramic strips, which were held in a mould. The polyurethanes were allowed to cure at ambient temperature for 24 h before a final 4-hour heat treatment in a furnace at 65 °C to ensure the polymers had fully cured. After curing, the top of the polymer was cut flat using a CNC mill, creating a level polymer backing with approximate dimensions of $60 \times 10 \times 5$ mm. Digital image correlation (DIC) was used to track the displacement field on the specimen surfaces; to enable this, a black and white speckle pattern was painted on the specimens using an airbrush. This speckle pattern was imaged during loading, and commercial DIC software, MatchID [23], was used to calculate the resulting displacements.

Further specimens were produced using glass-fibre reinforced polycarbonate bonded to the ceramic using Dowsil 6–1104. For these specimens, once the adhesive was applied, the specimens were held in a press for 72 h until fully cured.

3. Experimental overview

3.1. Quasi-static beam bend

Beam bend specimens were tested in 3-point bend at 0.05 mm/s at ambient and sub-ambient temperatures as presented in Table 1. The sub-ambient temperatures were selected using time-temperature superposition to achieve two separate conditions: -49 °C for Task 3 and Task 11 to simulate impact loading by replicating the polymer stiffness expected on timescales of approximately 1 μs ; -36 °C for Task 11 to mimic

Table 2
Experimental specimen variation for impact beam bend experiment.

Specimen Type	Backing	Bonding Condition
1	None	–
2	Task 3	Direct Curing – Primer and non-primer pre-treatment
3	Task 11	Direct Curing – Primer and non-primer pre-treatment
4	Task 3	Bonded – Low Strength – Pritt-Stick®
5	Task 11	Bonded – Low Strength – Pritt-Stick®
6	Task 3	Bonded – Dowsil 6–1104
7	Glass filled PC	Bonded – Dowsil 6–1104

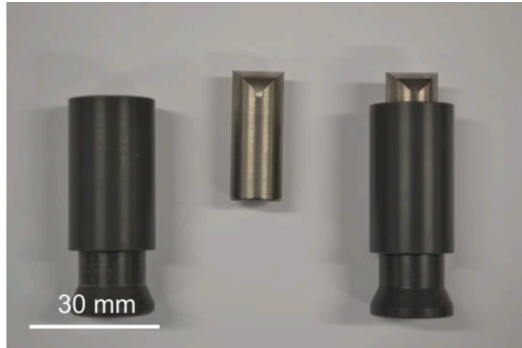


Fig. 3. Projectile and sabot used for impact beam bend.

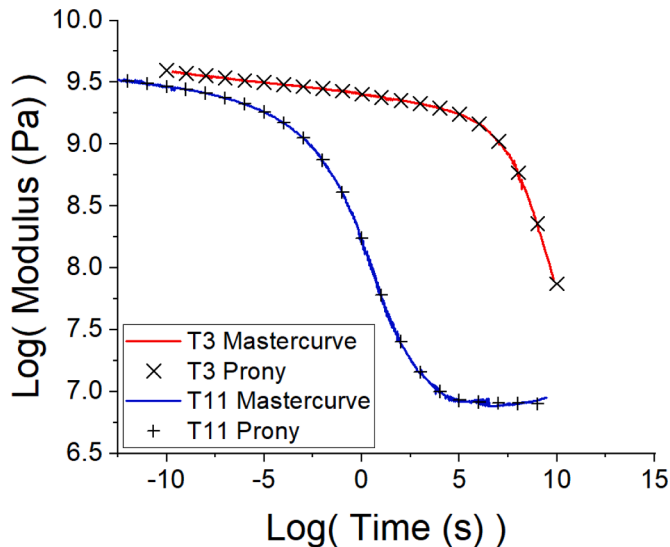


Fig. 4. Three-point bend DMA stiffness mastercurve for Task 3 and Task 11.

the stiffness of Task 3 at room temperature. Specimens were imaged with a Point Grey GS3-U3–41C6M-C camera allowing DIC analysis to accurately determine the central point deflection as well as observation of the resulting fracture patterns. The DIC parameters and camera settings can be found in the Appendix.

3.2. Impact beam bend

A single stage compressed nitrogen gas gun was used to investigate the performance of the specimens under impact, Fig. 2. Specimen variation was introduced as presented in Table 2. As well as the directly cured PU backings, specimen types 2 and 3, additional experiments were

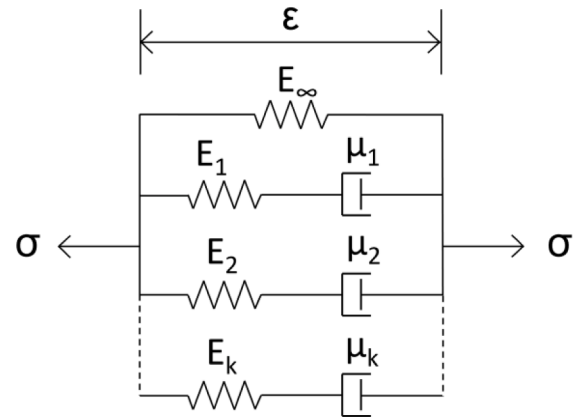


Fig. 5. Schematic representation of a Prony series.

conducted investigating a very low strength interface in which the backing was weakly bonded to the polymer using a small amount of commercially available paper adhesive, Pritt-Stick®, on specimen types 4 and 5. This allowed separation of the effect of interfacial strength from that of the backing's inertia. Further experiments were conducted using the silicone based adhesive Dowsil 6–1104 to delay interfacial fracture for Task 3 and the significantly stiffer glass filled polycarbonate, specimen types 6 and 7.

The specimens were set up as shown in Fig. 2 and were impacted using an EN16 steel projectile of 8 mm diameter and 30 mm length. The projectile had a cylindrically rounded tip of 4 mm radius, Fig. 3. A Photron Fastcam SA-Z high speed camera was used to record images of the impact at a rate of 100,000 fps; these images were used to obtain the specimen deformation and the speed of the projectile. A light gate was used to trigger the camera and determine the projectile speed before impact.

4. Polymer properties

4.1. Stiffness

Extensive mechanical characterisation of the polymers was performed in [21]. Of particular relevance here is the DMA characterisation of the small strain viscoelastic response. DMA specimens were loaded using a stress-relaxation testing procedure in a three-point bend configuration. Specimens were loaded slowly to 0.1% strain and held for 10 minutes, during which time the force was measured. The specimens were then allowed to recover, unloaded, for a further 20 min. This was repeated from -85 to +55 °C in 5 °C intervals. The principal of time-temperature superposition [24] was used to generate the 20 °C mastercurves shown in Fig. 4.

These results show that, in the range of interest for both polymers, the only transition is the glass transition, Fig. 4. The glass transition temperature was also confirmed using DSC, in which both materials were heated from -90 ° to 120 °C at a heating rate of 3 °C min⁻¹; the glass transition temperature was found to be at approximately 50 °C for Task 3 and 15 °C for Task 11. The full DSC results are presented in the Appendix.

From the DMA results, Fig. 4, it was observed that Task 3 was always stiffer than Task 11. In particular, under quasi-static loading, for which log(t)≈1, Task 3 was approximately two orders of magnitude stiffer than Task 11 and substantially less strain rate sensitive. Under impact loading conditions, log(t)≈6, the polymer stiffnesses converge and have similar sensitivity to strain rate. Thus, the use of two polymers allows an investigation into the effects of the glass transition on the response. Additionally, it was noted that the stiffness of the polymers converges at short timescales, which was expected due to their chemical similarity. It is also expected that the stiffnesses would converge at very long

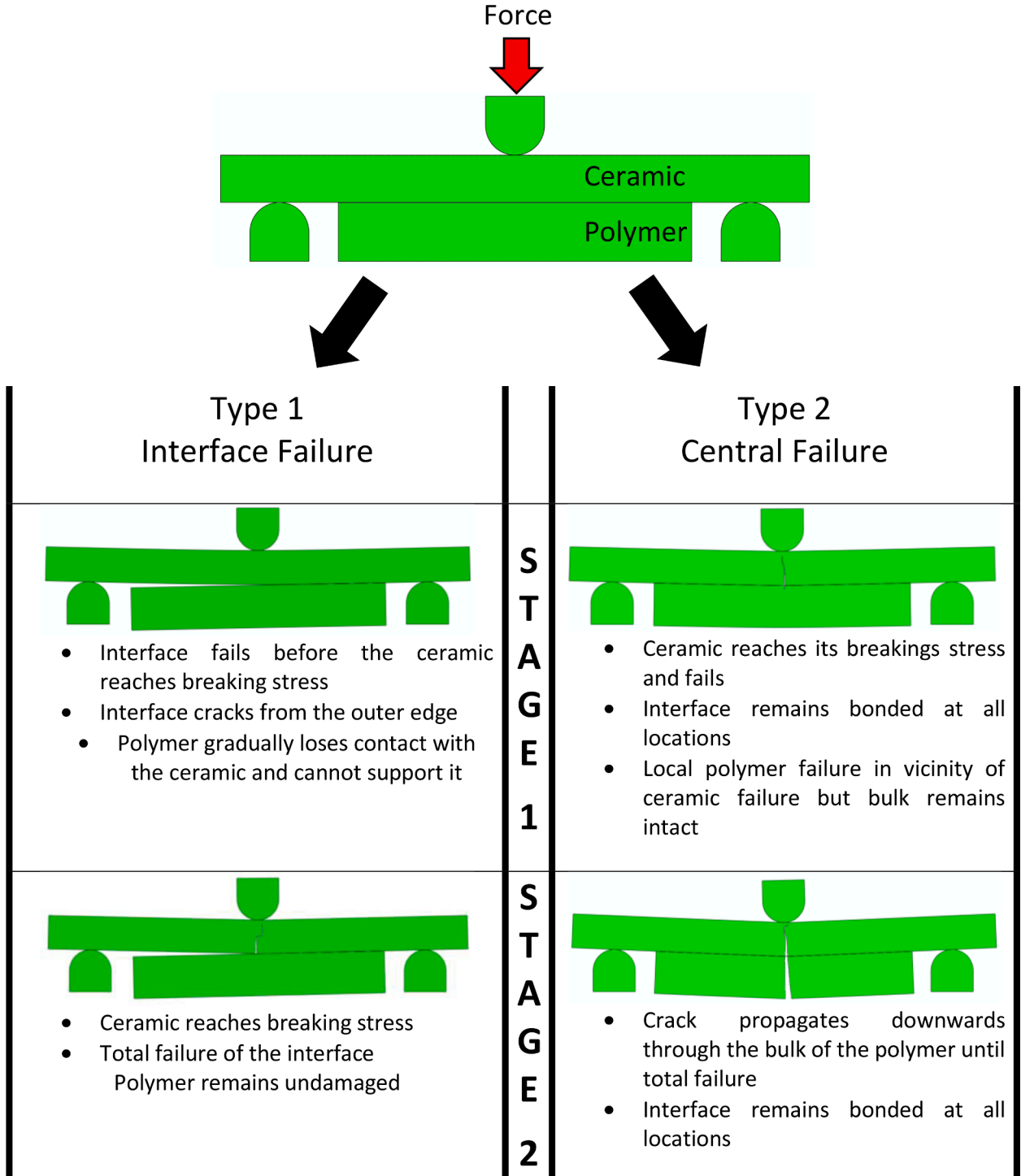


Fig. 6. Schematics of Type 1 and Type 2 failure.

timescales; however, data were not obtained as this is not of direct interest to the current research.

4.2. Modelling

A Prony series was used to model the polymers. A Prony series consists of a number of spring-dashpot pairs in parallel, each with different stiffness and relaxation time and each known as a branch, Fig. 5.

To determine the constitutive behaviour for this Prony series representation, a force balance along each branch should be taken and then a

Laplace transform with the particular initial conditions applied, [25,26]. For a step strain input, ϵ_0 , the stress relaxation behaviour can be represented by

$$\frac{\sigma(t)}{\epsilon_0} = G(t) = G_\infty + \sum_{n=1}^k G_n e^{-\frac{t}{\tau_n}} \quad (1)$$

where,

$$\tau_n = \frac{\mu_n}{E_n} \quad (2)$$

Here, G_n is a constant found from model parameters [25] and E_n and

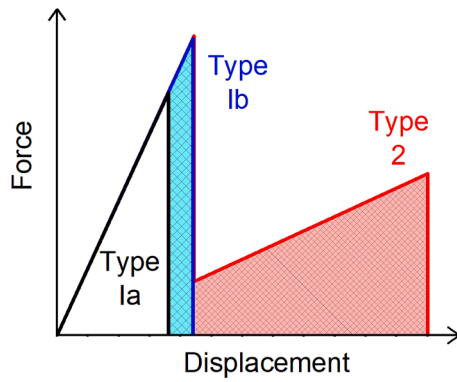


Fig. 7. Typical Force-displacement curves for Type 1 (Interfacial failure) and Type 2 (central failure). The shaded areas represent the additional load carrying capacity from each failure type.

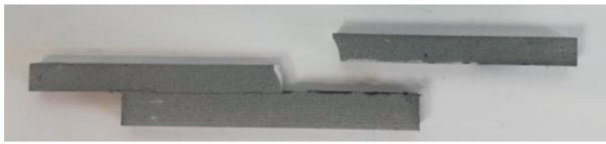


Fig. 8. Type 1- Interfacial failure of a composite bend specimen. Specimens have been painted to allow DIC to be performed.

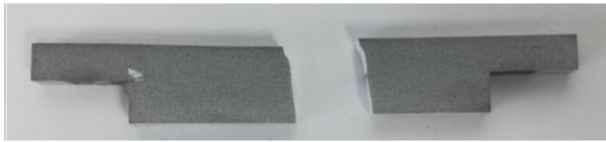


Fig. 9. Type 2 - Central failure of a composite bend specimen. Specimens have been painted to allow DIC to be performed.

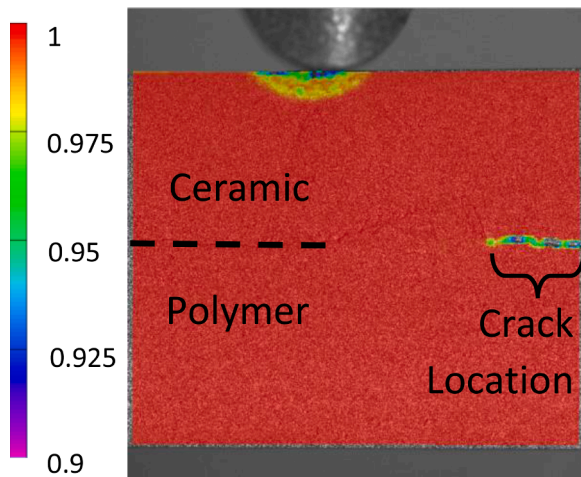


Fig. 10. Type 1 (interfacial failure) of a composite bend specimen using DIC to calculate the correlation coefficient map. The crack has propagated along the interface of the specimen from the right.

μ_n are the spring stiffness and dashpot viscosities, respectively, for each branch. The complexity increases for more general loading cases because the relaxation of the model will begin as soon as the loading starts. Therefore, for a general case

$$\sigma(t) = \varepsilon(0+) G(t) + \int_0^t G(t-s) \dot{\varepsilon}(s) ds \quad (3)$$

To define the Prony series representation of these polymers, Eq. (1) was fitted to the DMA mastercurves using the curve fitting toolbox in Matlab®. The number of branches was defined such that the characteristic time constant of each branch, defined by Eq. (2), was spaced by one decade. For Task 3 and Task 11, a 22-branch and 24-branch Prony series were fitted respectively. The predicted moduli at each loading decade are overlain on the mastercurve in Fig. 4, and the Prony series parameters used are presented in Table D.1.

5. Results and discussion

5.1. Quasi-static beam bend

5.1.1. Failure modes

Unbacked ceramic was initially tested to determine its inherent range of response. A Weibull analysis was conducted and the ceramic was found to have a Weibull modulus of 17.1, see the Appendix for details. The Task 3 and Task 11 backings were moulded to the ceramic specimens as previously described with and without a primer surface pre-treatment. It was observed that all specimens failed via two distinct modes schematically displayed in Fig. 6, and these gave the characteristic force-displacement curves presented in Fig. 7.

5.1.1.1. Type 1 - Interface failure. The first failure mode was termed interface failure. A characteristic of this failure was that the interface was observed to fail before either of the constitutive materials. A crack was observed to propagate from the outer edge of the ceramic-polymer bond and, thus, the ceramic gradually lost adhesion from and support of the polymer backing. Following this, once the ceramic reached its failure stress, the ceramic crack and the interfacial crack combined and the whole structure lost load carry capacity. This produced the typical force-displacement curve, Fig. 7, in which there was a single peak at the moment of ceramic failure.

This failure could be split into two further sub-divisions depending on how far the initial interfacial crack propagated along the specimen at the moment of ceramic failure. If the crack had propagated to the centre of the specimen, the ceramic behaved as if it were unbacked. This failure was denoted failure type 1a and these specimens were effectively indistinguishable from the unbacked ceramics.

In other cases, denoted type 1b, the ceramic failed before the interfacial crack reached the centre, such that it was still partially supported by the polymer. This increased the breaking stress in the ceramic, and also moved the failure away from the centre of the ceramic to the location of the interface crack tip. Because this location has a lower bending moment for any given force, the force required to fail the ceramic is increased, allowing the structure to survive to greater loads and displacements, see blue line in Fig. 10. After the ultimate failure of the ceramic, the ceramic crack and debonded interface still combined, resulting in the total failure of the specimen. This phenomenon, the polymer backing allowing the ceramic to withstand greater breaking stresses, has been previously observed under simulated ballistic impact [28]. When this failure was observed to occur, the energy absorption was observed to increase by approximately 1.5 – 1.8 times that of the unbacked ceramic.

5.1.1.2. Type 2 – central failure. The key characteristic for a type 2 failure was that no interfacial failure was observed to occur or, if any interfacial failure was present, it was limited to the farthest edges of the ceramic-polymer interface and did not affect the subsequent failure of the materials. The polymer remained fully bonded and was able to support the ceramic to greater breaking stresses, akin to those observed

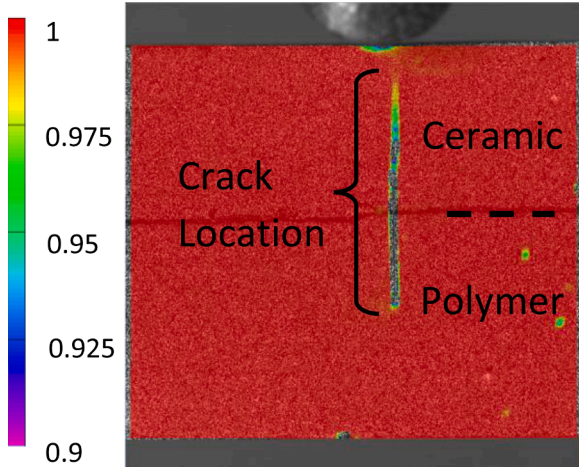


Fig. 11. Early stages of Type 2 (central failure) of a composite bend specimen using DIC to calculate the correlation coefficient map.

in type 1b. However, after the ceramic failed, the polymer remained bonded to the two halves of the ceramic section, allowing the system to withstand further load and resulting in a second peak in the force-displacement curve, Fig. 7, at which the polymer fractured via a second crack propagating from the interface. This additional loading secondary peak resulted in a substantial increase in energy absorption to approximately 3 times that of the unbacked ceramic.

5.1.1.3. Experimental observations. Type 1 and 2 behaviours were captured by observation during the loading, and are illustrated by images of failed specimens in Fig. 8 and Fig. 9. The failures could be observed visibly, but more accurately by using DIC to detect the crack paths during loading. One output of the DIC systems is a parameter called the correlation coefficient, which provides an indication of the similarity between images and can be used to detect fracture. As a crack propagates across an image, it produces significant local distortion of the image, resulting in a reduced value of the coefficient. Full-field maps of the correlation coefficient for a type 1 and a type 2 failure are presented in Fig. 10 and Fig. 11. Fig. 10, taken moments before total failure, clearly shows a crack along the interface. Once the ceramic fails, the ceramic crack and interfacial crack combine to produce the Type 1 failure in Fig. 8. Fig. 11 shows an image in the moments after ceramic failure and shows that, despite the ceramic having failed, the polymer remained bonded, which is consistent with the specimen continuing to support

load. No failure of the interface was detected in the centre of this specimen. The crack in the polymer propagated downward until total failure of the polymer, producing the specimen in Fig. 9.

5.1.2. Results

The normalised force-displacement results are presented in Fig. 12 and Fig. 13. To account for geometric differences, the force was normalised using the combined second moment of area and stiffness of the ceramic and backing. This was performed using

$$\hat{F} = \frac{F}{E_c I_c + E_p I_p} \quad (4)$$

Where \hat{F} is the normalised force, and E and I are the modulus and second moment of area respectively for the ceramic and polymer. The second moment of area of the polymer was calculated using the parallel axis theorem assuming that the neutral axis remains in the centre of the ceramic. In fact, the addition of the polymer backing moves the neutral axis, but the differences in stiffness are large and this effect was therefore calculated to be negligible.

At room temperature for Task 3 (green), Fig. 12, both the primer and non-primer surface treatment displayed type 2 failure, resulting in the characteristic double peak response in the force-displacement graph. Further, the maximum breaking force in the ceramic was consistently observed to be greater than that of the unbacked ceramic. For these specimens, the addition of the primer allowed for specimens exhibiting greater ultimate failure displacement over those bonded without this surface pre-treatment. When the temperature was reduced to -49°C (red/orange), the failure mode became, generally, type 1b, in which the interface was observed to fail before the ultimate failure of the ceramic, but the polymer was still sufficiently bonded to the ceramic to allow the breaking stress of the ceramic to increase over the unbacked ceramic. At these temperatures, the surface prepared in the absence of a primer, was generally observed to increase the ultimate failure displacement of the specimens over those specimens bonded with the primer. It was thought that the increased complexity of the interface from the presence of the primer at sub-ambient temperatures caused a general weakening of the interface.

For Task 11, at room temperature Type 2 failure was observed to occur, although due to the ductility of this polymer this was the extreme of this classification of behaviour. Whilst there was relatively little increase in the ceramic breaking stress, there was a significant increase in ultimate failure displacement as neither the interface nor polymer failed for a considerable time. Under this loading, the primer surface treatment was observed to reduce the ultimate failure displacement considerably.

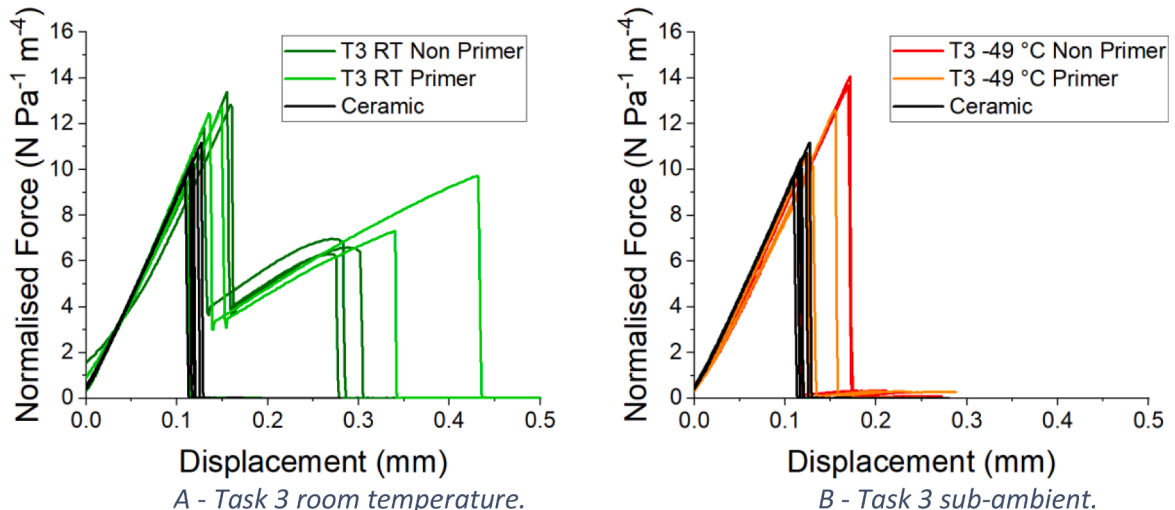


Fig. 12. Force vs displacement response for Task 3 under quasi-static loading conditions split into the room temperature and low temperature experiments.

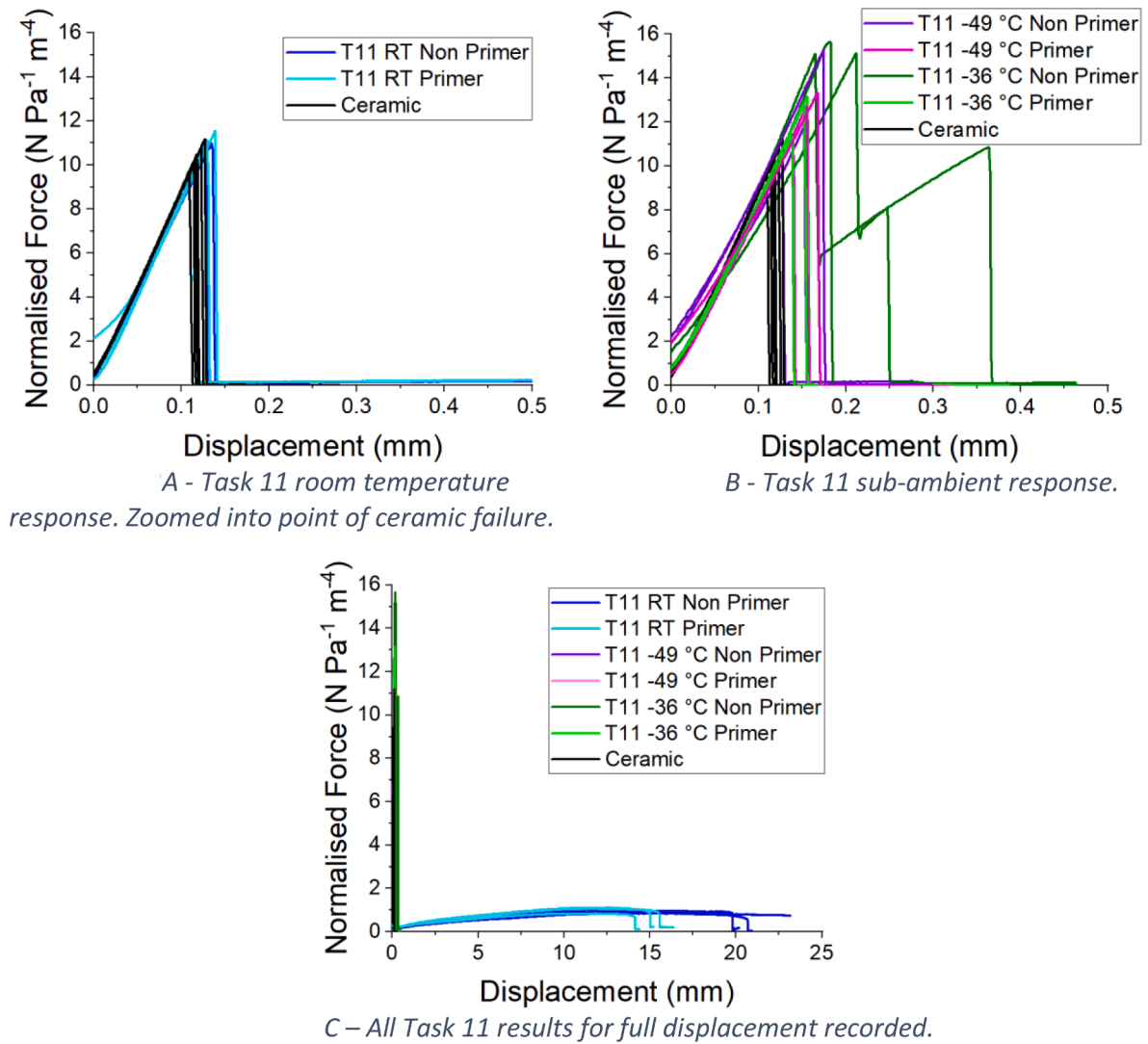


Fig. 13. Force vs displacement response for Task 11 under quasi-static loading conditions. Task 11 -36 °C and Task 3 room temperature share the same colour scheme (green) as these conditions were chosen to mimic each other.

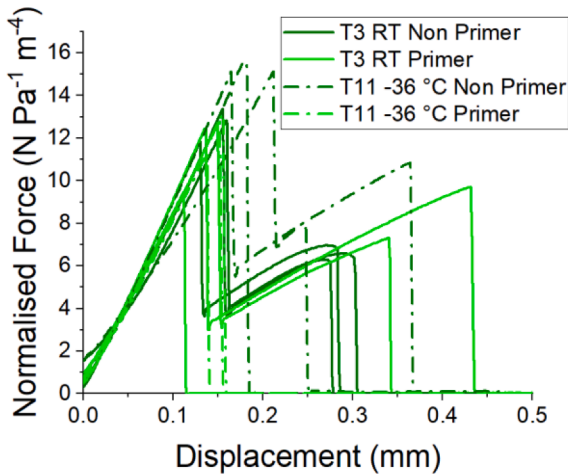


Fig. 14. Comparison between Task 3 and low temperature Task 11. The temperature was chosen to give the similar polymer stiffness between the polymers.

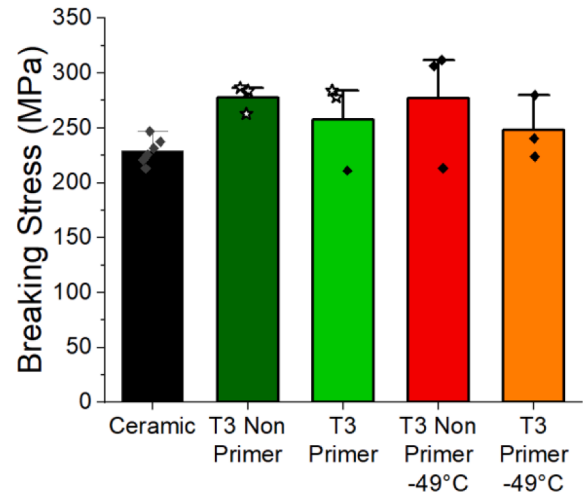


Fig. 15. Breaking stress in the ceramic for ceramic bend specimens backed with Task 3. Diamonds denote Type 1 failure and stars, Type 2.

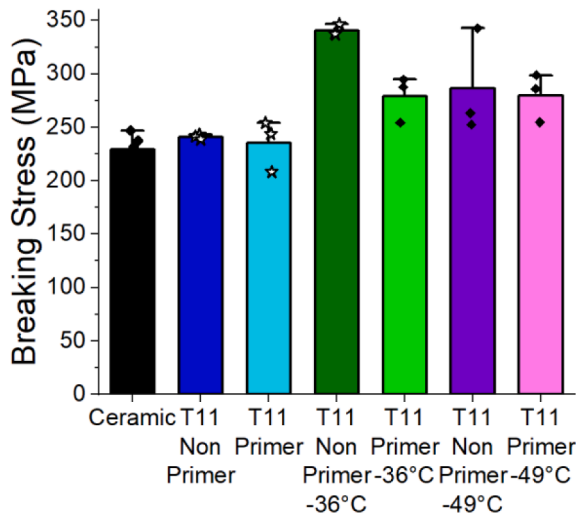


Fig. 16. Breaking stress in the ceramic for ceramic bend specimens backed with Task 11. Diamonds denote Type 1 failure and stars, Type 2.

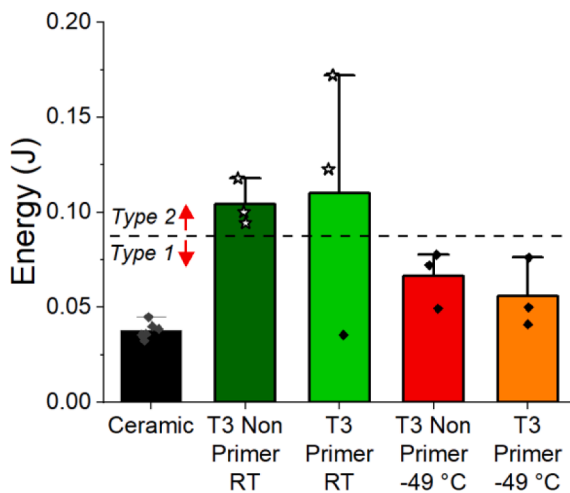


Fig. 17. Energy absorbed during loading for Task 3. Diamonds denote Type 1 failure and stars, Type 2.

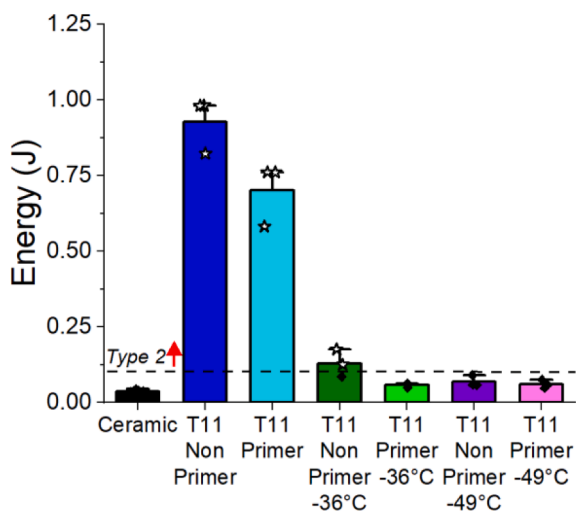


Fig. 18. Energy absorbed during loading for Task 11. Diamonds denote Type 1 failure and stars, Type 2.

Once unloaded, all deformation of the polymer was fully recoverable. When the temperature was reduced to -49°C (purple/pink), Type 1b failure now occurred. The breaking stress was found to have been increased over that of the unbacked ceramics, and the influence of the primer/non-primer surface treatment on the breaking stress was similar. At -36°C , where the temperature was selected to mimic the polymer response of Task 3 at room temperature, there was a re-emergence of the Type 2 failure mode very similar to that exhibited by Task 3, Fig. 14, which suggests this behaviour can be controlled through polymer stiffness as well as the interfacial strength. Interestingly, those specimens bonded with a primer pre-treatment all failed in the Type 1b failure mode. This suggests the difference between Type 1 and Type 2 fails is a relatively fine threshold and differences such as the use of a primer pre-treatment or not can have significant effects on the overall specimen response. This subsequently would have a significant influence on the overall energy absorbing capacity of the specimen.

The breaking stress in the ceramic at the point of failure, calculated using beam bend theory, is displayed in Fig. 15 and Fig. 16, and the energy absorbed during loading, calculated as the area under the force-displacement curve, is presented in Fig. 17 and Fig. 18. In these graphs, black diamonds represent Type 1 failure and stars represent Type 2. Whilst there was relatively little influence of the failure mode type on the breaking stress, it had a significant influence on the energy absorption capability of the specimens and significantly more energy was absorbed when the specimens failed in the Type 2 failure mode compared to Type 1. These results are tabulated in Table 3. When failure Type 1b was present, there was an approximate increase in energy absorption by a factor of 1.5 – 1.8 over that of the unbacked ceramics. When specimens failed under Type 2, the increase was on the order of a factor of 3, aside from the ductile Task 11 under ambient conditions, which absorbed approximately 20 times as much energy as the unbacked ceramic. Therefore, if the threshold between Type 1 and 2 behaviour could be better understood and controlled the increase in energy absorption capability could be significant.

One final consideration was the influence of thermal contraction on the specimens. Because there is approximately an order of magnitude difference in the coefficient of thermal expansion for alumina ($\sim 1.3 \times 10^{-5} \text{ K}^{-1}$) and polyurethane ($\sim 2 \times 10^{-4} \text{ K}^{-1}$), upon contraction thermal strains were likely to develop over the interface. To determine this influence, speckled specimens were cooled from ambient temperature to -60°C and images were taken every second during the cooling process. DIC was performed on the resulting images to extract the displacement fields, Fig. 19 and Fig. 20. It was found that there was significant thermal strain across the PU-alumina interface, which resulted in thermally-induced interfacial failure. Here, failure was defined as the first point of detection of a discontinuity in the vertical displacement field at the edge of the interface. Specimens backed with Task 3 were observed to fail at approximately -10°C for both the primer and non-primer specimens; those backed with Task 11 failed at approximately -40°C for the primer and non-primer, respectively, but the primer was generally found to debond $2-3^{\circ}\text{C}$ earlier. This shows that the use of time-temperature superposition here would likely cause a different specimen behaviour than the dynamic loading it was aiming to simulate. However, the conclusions above on the energy absorption capabilities of the specimen due to the failure modes and their sensitivity to stiffness and interfacial performance are still valid.

5.2. Impact beam bend

5.2.1. Task 3 and 11 - Primer vs non-primer

Results for impact beam bend experiments for Task 3 and Task 11 are presented in Fig. 21, in the form of incident vs residual speed. The speeds were calculated from tracking the projectile through images, determining the number of pixels traversed in a known time and converting this to speed using the known pixel to mm conversion. All the results displayed a relatively linear relationship between the incident and

Table 3

Energy absorbed for each loading condition.

			Mean energy absorbed (J)	Improvement factor vs. unbacked ceramic	Failure mode type
Ceramic			0.038	–	–
Task 11	RT	Non Primer	0.93	24.5	Type 2
		Primer	0.70	18.5	Type 2
	-36 °C	Non Primer	0.13	3.4	2× Type 2, 1× Type 1
		Primer	0.06	1.6	Type 1
	-49 °C	Non Primer	0.06	1.6	Type 1
		Primer	0.070	1.8	Type 1
Task 3	RT	Non Primer	0.10	2.8	Type 2
		Primer	0.11	2.9	2× Type 2, 1× Type 1
	-49 °C	Non Primer	0.066	1.8	Type 1
		Primer	0.056	1.5	Type 1

residual speed across the range of speeds tested as would broadly be predicted by the Lambert-Jonas relation above the ballistic limit [29, 30]. In general, the addition of the polymer backing produces approximately a 30% reduction in absolute speed over the unbacked ceramic specimens.

Comparing the primer and non-primer pre-treatments, for Task 3 there was an improvement of approximately 10% from the addition of the primer pre-treatment but minimal improvement for the Task 11 polymer. The mechanism for this performance improvement was

believed to be observed in the failure, Fig. 22 and Fig. 23. From observation of fracture pathways, cracks originating from the point of impact spread in a conical pattern typical of ballistic impact [4]. Once these cracks reach the polymer interface, they either pass directly across the boundary into the polymer or propagate along the interface. Generally, it was observed that the interfaces pre-treated with a primer inhibited crack growth along the interface. Instead, cracks grow more slowly into the polymer, which allows the polymer to support the ceramic for longer and absorbs more energy for the same amount of crack elongation. This

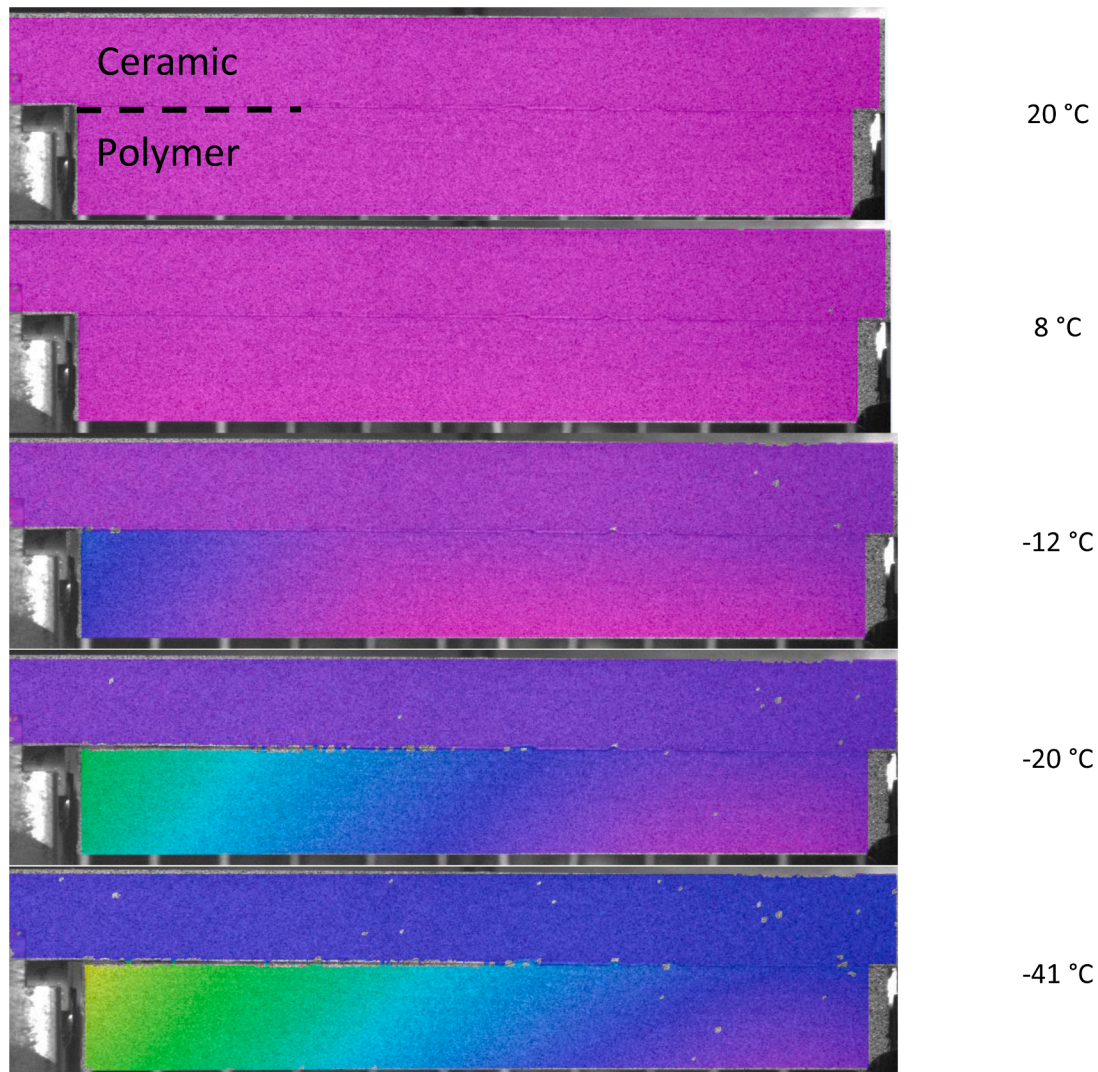


Fig. 19. DIC vertical displacement map for Task 3 backed alumina for select images for the primer backed specimens. Failure from thermal contraction was observed.

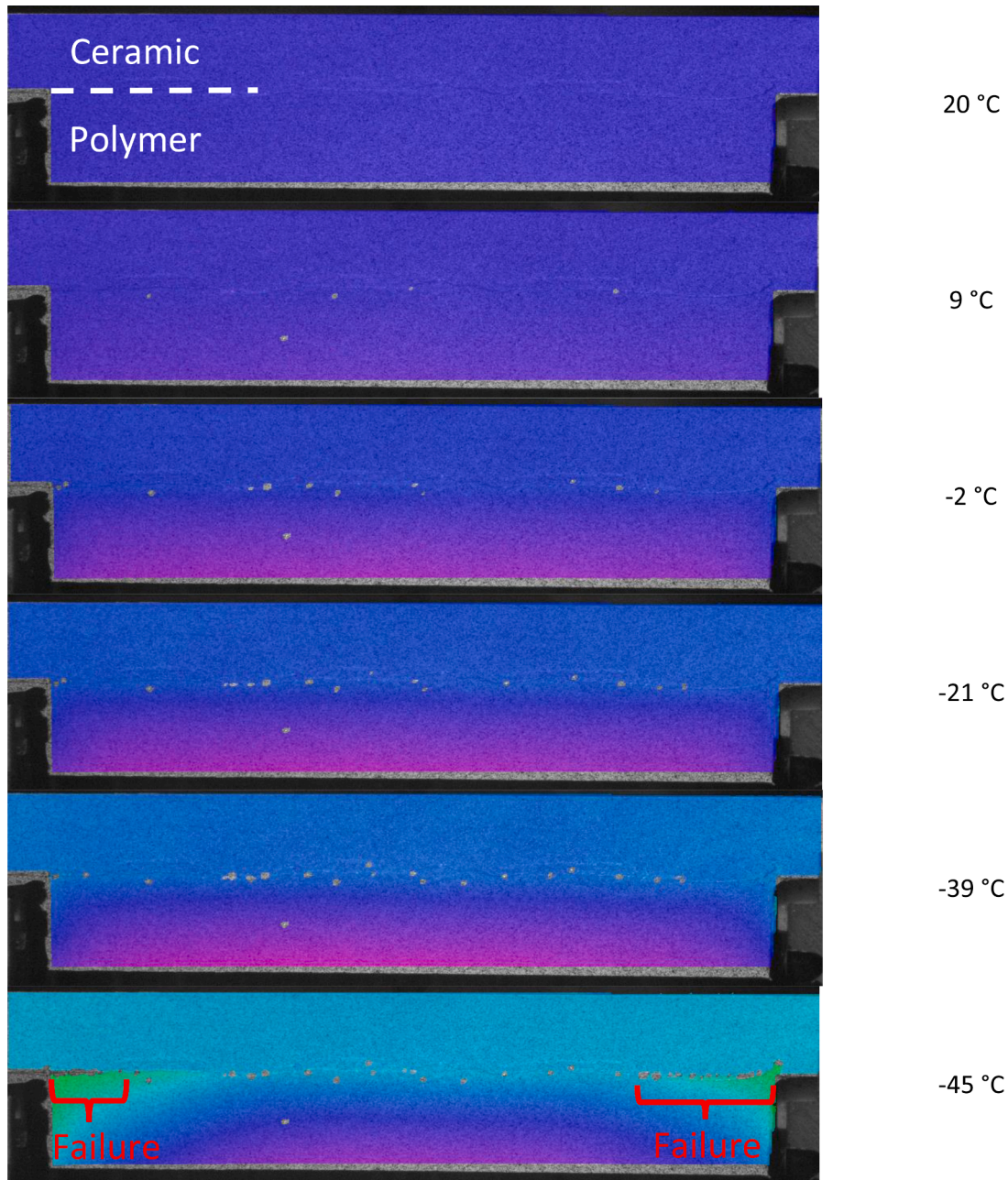


Fig. 20. DIC vertical displacement map for Task 11 backed alumina for select images for the primer backed specimens. Failure from thermal contraction was observed.

was opposed to debonding and cracking directly along the interface which was generally observed in the Task 3 specimens without a primer pre-treatment. Further, polymers typically have a greater fracture energy compared to ceramics so any increased polymer fracture observed here would lead to greater energy absorption. This behaviour has been highlighted in red in Fig. 22 compared to Fig. 23. This behaviour is akin to the previously observed Type 2 failure mode under quasi-static loading. This observed phenomenon highlights the benefits of this geometric experimental set up as such observations would be obscured in plate impact.

For Task 11, no measurable difference in performance was recorded between specimens with and without a primer pre-treatment. This was thought to be because, for each surface preparation type, there was no observed difference in failure mode, Fig. 24 and Fig. 25. Once the cracks,

propagating through the ceramics from the point of impact, reached the interface, the ductility of the polymer was such that no cracks could propagate into the polymer and instead chose to propagate along the interface. The energy release rate of these interfaces under dynamic loading were found to be similar [31] and so any energy absorption differences due to interfacial fracture would be small.

Inertial effects are significant in dynamic experiments; therefore, to allow a fair comparison to be made, the velocities can be replotted and normalised with respect to the total masses of the specimens, Fig. 26. Here it is shown that the mass normalised performance from the addition of the backing produced an improvement of ballistic performance on the order of 15% compared to the equivalent mass of ceramic.

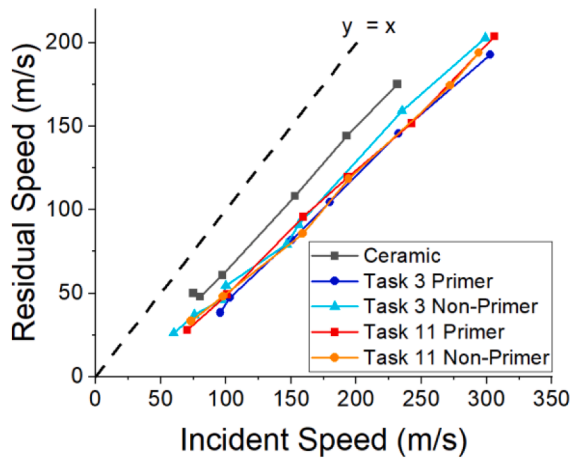


Fig. 21. Incident vs. residual speed during impact for Task 3 and Task 11 with and without a primer pre-treatment. The line of $y = x$ is shown for reference.

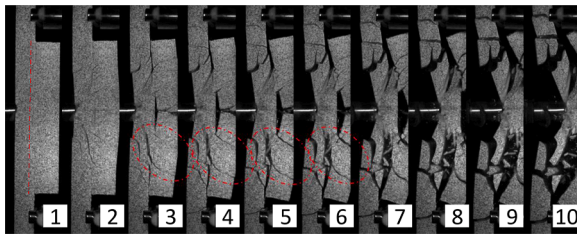


Fig. 22. Task 3 beam bend impact at 100 m s^{-1} with a primer surface pre-treatment. The polymer-ceramic boundary is shown in image 1 with the ceramic as the strike face. The region circles in red shows crack propagation across the interface into the polymer. Image 1 is at the moment of impact and subsequent images are shown every $20 \mu\text{s}$.

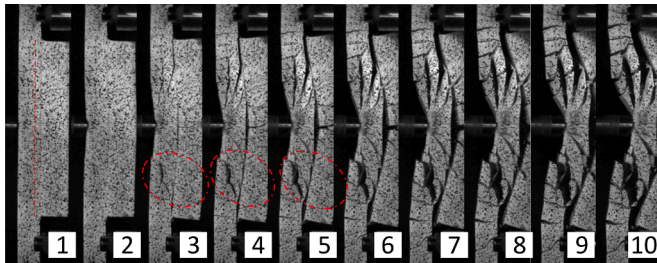


Fig. 23. Task 3 beam bend impact at 100 m s^{-1} without a primer surface pre-treatment. The polymer-ceramic boundary is shown in image 1 with the ceramic as the strike face. Image 1 is at the moment of impact and subsequent images are shown every $20 \mu\text{s}$.

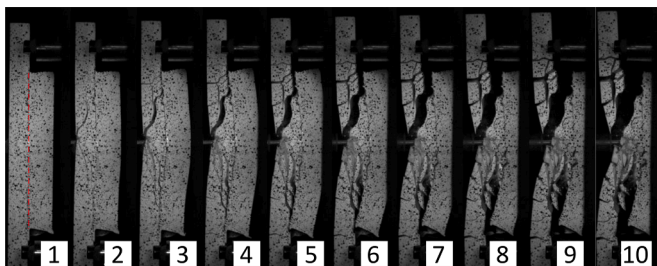


Fig. 24. Task 11 beam bend impact at 100 m s^{-1} with a primer surface pre-treatment. The polymer-ceramic boundary is shown in image 1 with the ceramic as the strike face. Image 1 is at the point of impact and subsequent images are shown every $20 \mu\text{s}$.

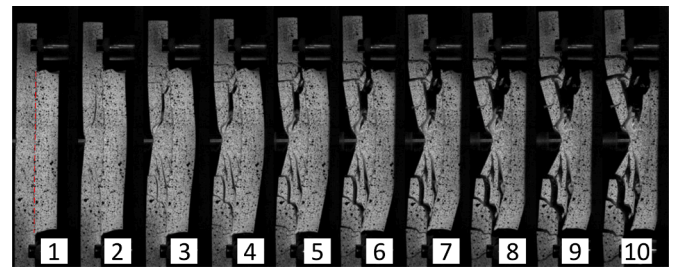


Fig. 25. Task 11 beam bend impact at 100 m s^{-1} without a primer surface pre-treatment. The polymer-ceramic boundary is shown in image 1 with the ceramic as the strike face. Image 1 is at the point of impact and subsequent images are shown every $20 \mu\text{s}$.

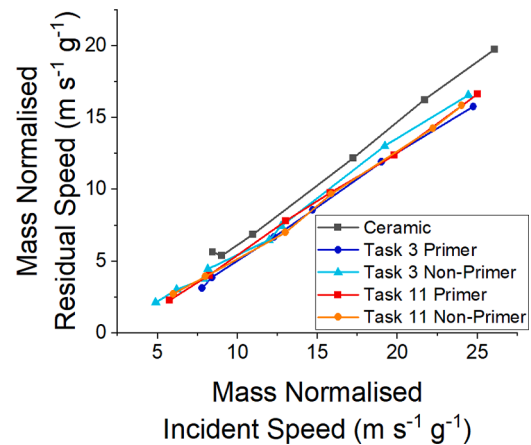


Fig. 26. Mass normalised incident vs residual speed for Task 3 and Task 11 for primer and non-primer pre-treatment.

5.2.2. Further specimen types

5.2.2.1. Strengthless interface. Considering the differences in behaviour, it is interesting that the overall impact performance of specimens made using the two polymers was similar. It was hypothesised that a significant portion of the incident kinetic energy was being converted to kinetic energy of the fragments and not absorbed by material deformation. Therefore, to separate the difference between the interfacial and inertial effects, a further experiment was conducted in which polyurethane backings were cured separately and then lightly adhered to the alumina using Pritt-stick®. The consequence of this was a specimen in which the polymer was present behind the ceramic, but with almost zero interfacial strength.

Fig. 27 shows that the removal of interfacial strength has little effect on the overall armour performance. For Task 11 and Task 3, the strengthless condition produced very similar results to those above. This suggests that for these polymers and loading conditions, the transfer of kinetic energy to the material fragments is the significant energy absorption mechanism. Although the interface was previously observed to cause differences in the fracture pathways, for this experimental geometry, it was not a significant energy absorption mechanism but could be for more complex geometries and if the armour was used in front of a more representative material instead of free standing, e.g. ballistic gel. Such investigations were beyond the scope of this work.

5.2.2.2. Glass-fibre reinforced polycarbonate and Dowsil 6-1104. A final investigation was conducted into the influence of a stiffer polymer on the overall armour response. Glass fibre reinforced polycarbonate was bonded to the alumina using Dowsil 6-1104 and compared to Task 3 bonded with this adhesive. This is a silicone-based adhesive and is more

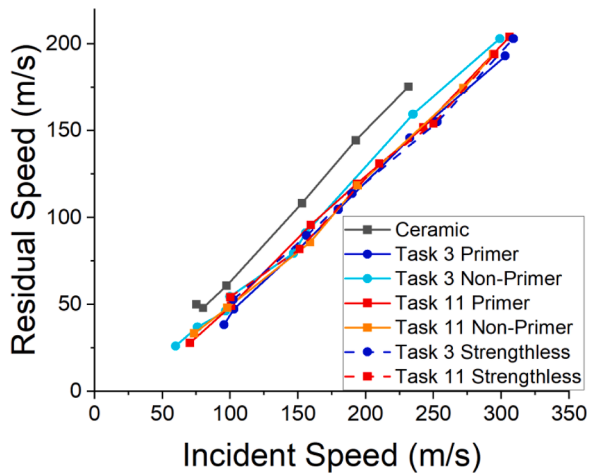


Fig. 27. Task 11 and Task 3 residual vs incident velocities under primer and non-primer surface pre-treatments and strengthless interfaces.

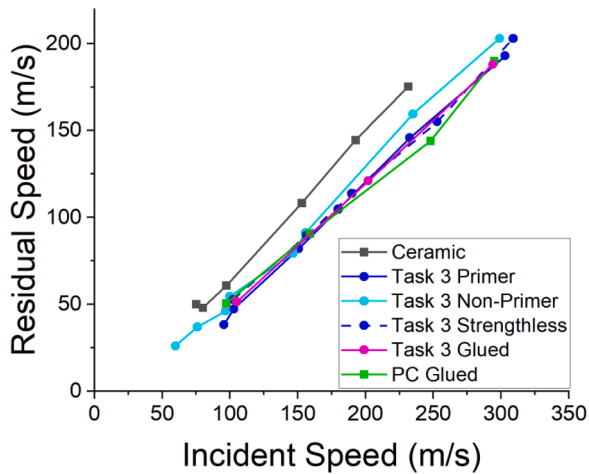


Fig. 28. Task 3 and PC residual vs incident velocities under primer, non-primer, strengthless and bonded interfacial conditions. The results from Task 11 have been removed for clarity.

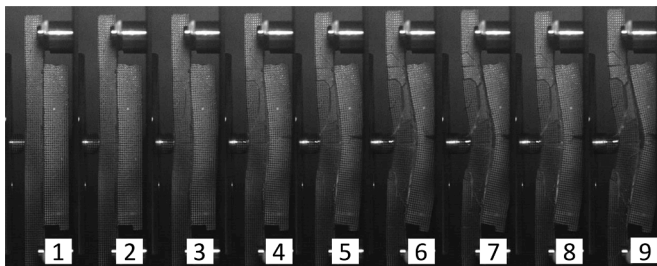


Fig. 29. Task 3 bonded with Dowsil 6-1104. Impact was at 100 m s^{-1} and each image is separated by $10 \mu\text{s}$.

ductile than the interface generated by the direct curing method but would allow the polymer to be bonded to the ceramic for a longer duration.

From the results obtained, Fig. 28, it appeared that using the material stiffness and interface ductility investigated here made little difference to the energy absorption. This was perhaps expected from observation of the fracture paths, Fig. 29 and Fig. 30. These specimens fail in a manner similar to that previously found with Task 11, Fig. 24, where no cracks passed from the ceramic into the polymer backing and all propagated

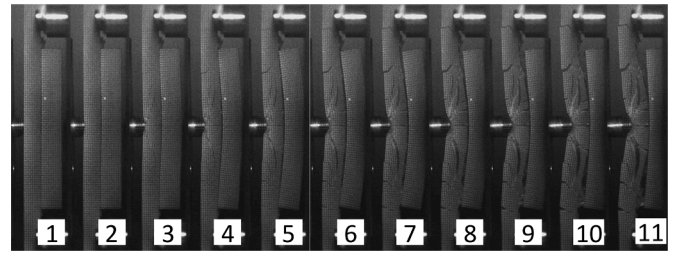


Fig. 30. GFPC bonded with Dowsil 6-1104. Impact was at 100 m s^{-1} and each image is separated by $10 \mu\text{s}$.

Table 4

Simulation parameters to model the response of steel.

Stiffness (GPa)	205
Poisson's Ratio	0.29
Density (kg m^{-3})	7870
Element Type	
(Quasi-static/Impact)	CPS4R/C3D8R
Element Size (mm)	0.5

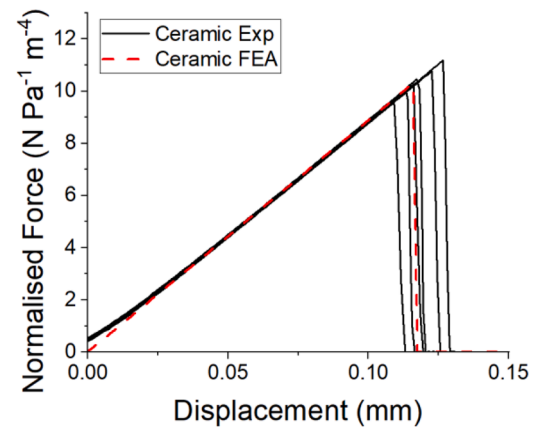


Fig. 31. Ceramic experiment vs FEA under quasi-static beam bend.

Table 5

Simulation parameters to model the response of alumina.

Stiffness (GPa)	270
Poisson's Ratio	0.21
Density (kg m^{-3})	3140
Failure Stress (MPa)	207
Post damage displacement (m)	1×10^{-5}
Element Type	
(Quasi-static /Impact)	CPS4R/C3D8R
Element Size (mm)	
(Quasi-static /Impact)	0.5/0.2

along the interface and so the energy absorption of this was similar.

6. FEA results

FEA simulations were performed in Abaqus 2021 to determine whether the observed behaviour of the specimens can be recreated using materials and interfacial properties that have been separately characterised. Under quasi-static loading, the results only simulated the beam bend response at room temperature as well as -49°C for Task 3 and -36°C for Task 11. The results for -49°C for Task 11 were not simulated because no interfacial characterisation from a separate study [31] was performed at this temperature.

A 2D static general model was used with an XFEM fracture definition

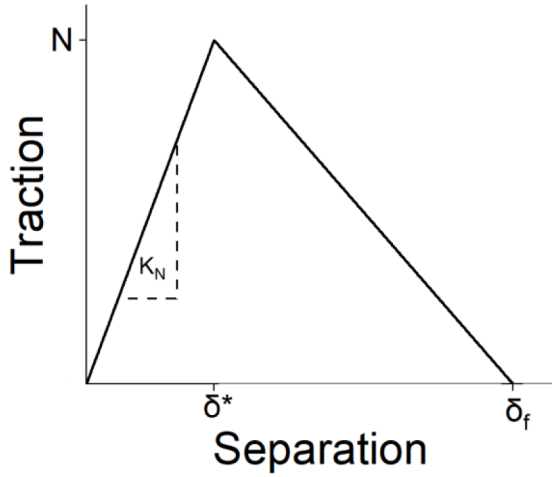


Fig. 32. Example TSL response.

to model the quasi-static behaviour. A 3D dynamic explicit model was used to capture the impact behaviour of the specimen.

6.1. Material models

6.1.1. Steel

The projectiles and specimen supports were manufactured out of EN16 steel and an elastic material model was used to represent their behaviour. The simulation parameters are presented in Table 4, with the material properties obtained from the material datasheet.

6.1.2. Alumina

To model the brittle failure response of the ceramic, an elastic material model was used which allowed XFEM crack growth under tensile stress. The model was calibrated against experimental data to reproduce the observed stiffness and breaking stress, Fig. 31. Damage was set to initiate at defined stress and, once this damage had initiated, a very short failure displacement was defined to allow for the brittle nature of the ceramic. The remaining material parameters, the density and Poisson's ratio, were found in the material datasheet. These simulation parameters are presented in Table 5.

6.1.3. Interface

6.1.3.1. Quasi-static response. To simulate the interfacial behaviour of the interface, a traction separation law (TSL) was used to populate cohesive elements in Abaqus 2021. To be able to model a propagating

Table 6
TSL parameter definitions.

			K_N (Pa m ⁻¹)	N (MPa)	δ_f (μm)
Task 3	RT	Non Primer 1	3.13×10^{13}	116	15.7
		Non Primer 2	1.03×10^{13}	62.0	14
		Primer 1	1.26×10^{13}	62.3	14
	-40	Primer 2	7.6×10^{12}	31.2	11.6
		Non Primer 1	1.21×10^{14}	447	16
		Primer 1	3.68×10^{12}	20.6	16.6
Task 11	RT	Primer 2	2.5×10^{12}	32.5	25.4
		Non Primer 1	2.32×10^{13}	267	25.9
		Non Primer 2	1.25×10^{13}	173	29.9
	-22	Primer 1	7.79×10^{12}	126	42.7
		Non Primer 1	8.19×10^{12}	120	30.9
		Non Primer 2	1.42×10^{13}	142	21
		Primer 1	1.68×10^{13}	163	24.2

Table 7

Simulation parameters to model the response of Task 3 and Task 11 for a static general simulation.

	Task 3		Task 11	
	Room Temp	-49 °C model	Room Temp	-36 °C model
Stiffness (GPa)	2.3	3.2	0.64	2.3
Poisson's Ratio	0.49	0.49	0.49	0.49
Density	1120	1120	1120	1120
Failure Stress (MPa)	25	35	–	30
Post damage displacement (m)	1×10^{-5}	1×10^{-5}	–	1×10^{-5}
Ogden model	–	–	$\alpha = 10.9$ $\mu = 3.3$ MPa	–
Element Type	CPS4R	CPS4R	CPS4R	CPS4R
Element Size (mm)	0.5	0.5	0.5	0.5

Table 8

Simulation parameters to model the response of Task 3 and Task 11 for a dynamic explicit simulation.

Stiffness (GPa)	Prony Model *See Appendix
Poisson's Ratio	0.49
Density	1120
Element Type	C3D8R
Element Size (mm)	0.2

crack, this model makes use of the relation,

$$\sigma(\Delta) = \frac{dJ}{d\Delta} \quad (5)$$

where Δ is the opening displacement at the crack tip, σ is the traction

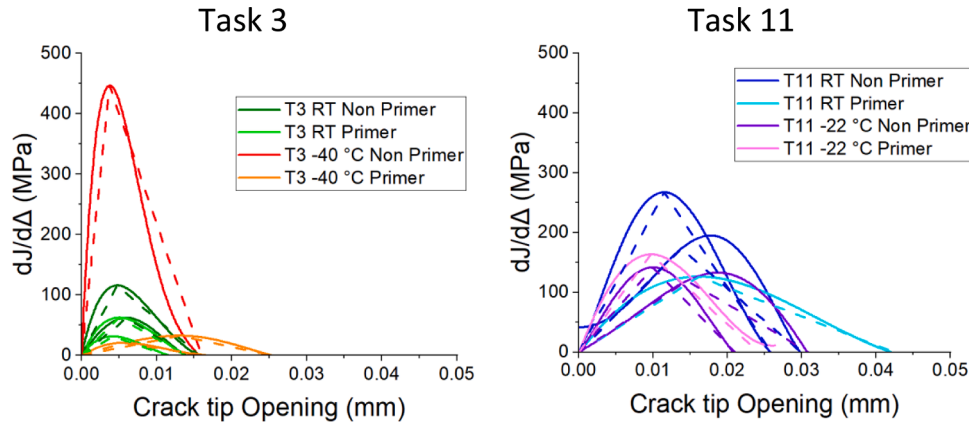


Fig. 33. Cohesive representation and TSL modelling of the PU-alumina interface for Task 3 and Task 11. The solid lines represent the experimental results and the dashed, the linear TSL fit.

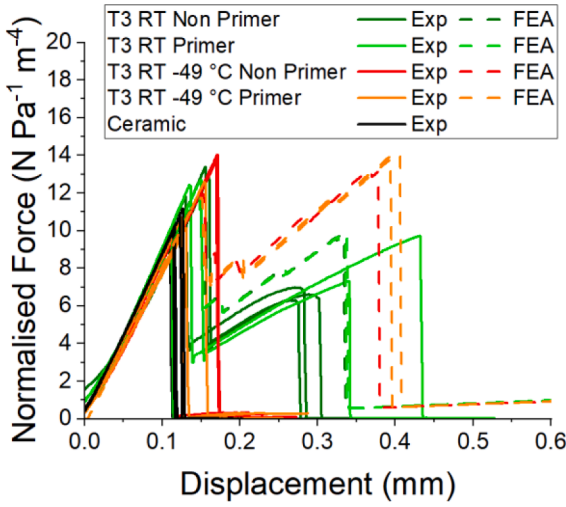


Fig. 34. Quasi-static beam bend experimental vs FEA results for Task 3.

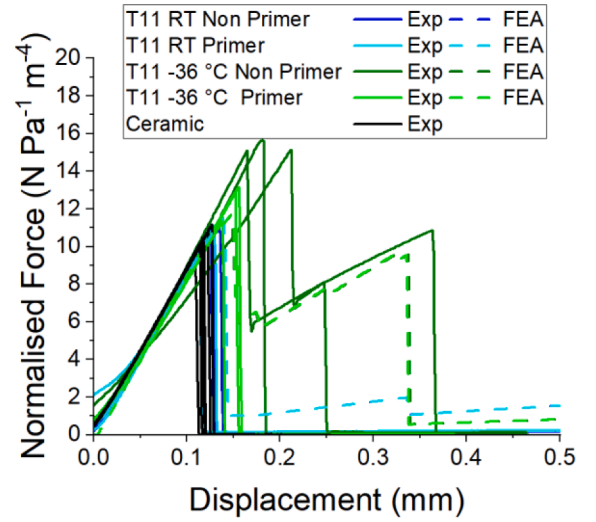


Fig. 36. Quasi-static beam bend experimental vs FEA results for Task 11.

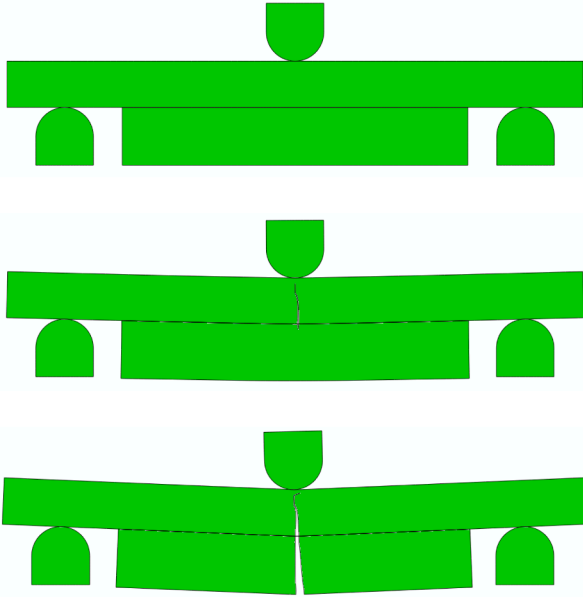


Fig. 35. Typical simulated failure mode for beam bend loading for alumina backed with Task 3 at ambient and sub-ambient conditions.

normal to the crack and J represents the J-integral, which is a measure of the energy availability to propagate the crack [32,33]. Therefore, if the evolution of the J-integral with tip opening displacement is known, then the behaviour of the crack can be modelled from the gradient of this relationship [34]. An idealised J-integral vs tip opening relation would start from zero, where the crack is fully closed, before rising to a critical steady state value where the crack is propagating, see [35] for a detailed description. Therefore, the gradient of this curve would rise to a peak before reducing, and this can be approximately represented by the relationship in Fig. 32. The behaviour of the element beyond δ^* , where the onset of damage begins, can take a variety of shapes; however, for this study, a linear damage evolution model was chosen.

The experimental response of the interfaces of interest to this study have been characterised in a previous study [31]. In this study, ceramic strips were bonded together using the polyurethanes of interest and a wedge driven between the two surfaces. The crack tip was imaged and the J-integral and tip opening displacement was determined for every timestep. This experimental relationship was determined, differentiated, and plotted as solid lines in Fig. 33. This was fitted to the linear TSL

representation, displayed as dashed lines in the figure, with the numerical definitions presented in Table 6. The cohesive elements from Task 11 were found to withstand greater forces in general than those from Task 3; however, this was thought to be an overestimation of reality due to the calculation of the J-integral for this polymer due to its increased ductility. For a full investigation of this consult [31].

Note, these experiments were performed at temperatures different to that previously discussed in this paper because these experiments were guided by a different set of DMA results, which produced a different set of shift factors. These were used to model the material response closest to the experimental conditions. For Task 11 this was -36°C , and therefore the material properties of the polymer were defined at these conditions.

6.1.3.2. Impact. Under dynamic explicit loading conditions, the accuracy of cohesive elements is known to be limited. Therefore, only the extremes of loading were investigated: modelling the interface as fully stuck and fully free. This was achieved within the interface definition by allowing it to separate, or not, under loading.

6.1.4. Polymer

6.1.4.1. Quasi-static response. The behaviour of the polymer was approximated from tensile tests on the materials. Similar to the ceramic material model, XFEM fracture was enabled with a short damage evolution displacement being defined to capture the brittle nature of this deformation. All polymers exhibited this behaviour, apart from Task 11 whose response was captured using an Ogden model. The values of these parameters are displayed in Table 7. The polymer stiffness was determined through DMA experiments and using TTS to determine the stiffness at the appropriate temperatures and timescales. The failure stress, post damage displacement and Ogden model parameters were determined through separate uniaxial tension experiments. The material density was found from the provided datasheets. The Poisson's ratio, ν , of these polymers was found through ultrasound experiments and the relation between the longitudinal, c_l , to the shear, c_s , wave speed defined as

$$\nu = \frac{c_l^2 - 2c_s^2}{2(c_l^2 - c_s^2)} \quad (6)$$

6.1.4.2. Impact response. The model of the polymer under impact loading shared similarities with the quasi-static model. However, the key difference was the polymers were now modelled using the Prony

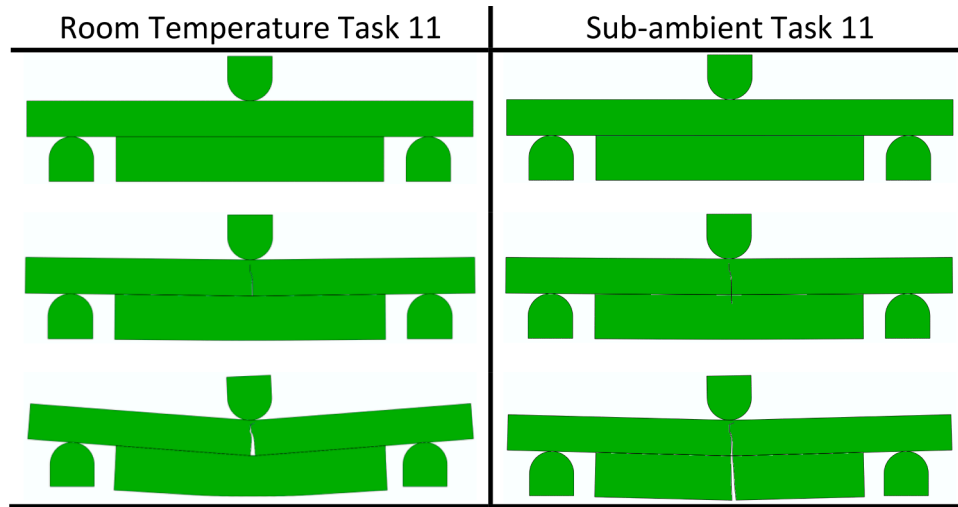


Fig. 37. Failure modes of Task 11 at ambient and sub-ambient conditions.

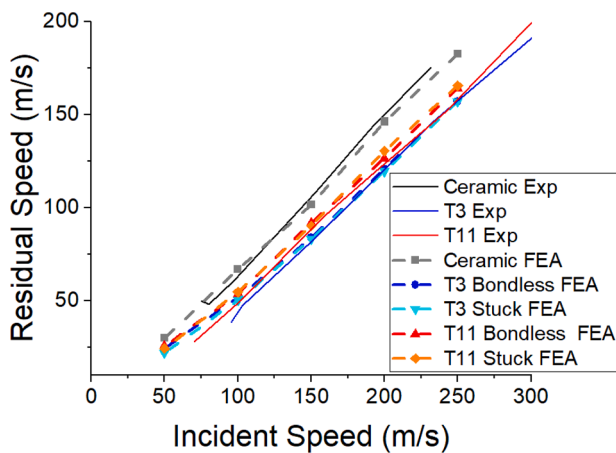


Fig. 38. Incident vs residual speeds comparing experiment (solid) to simulation (dashed) for impact beam bend.

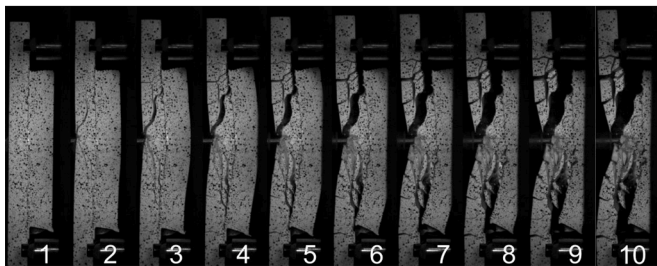
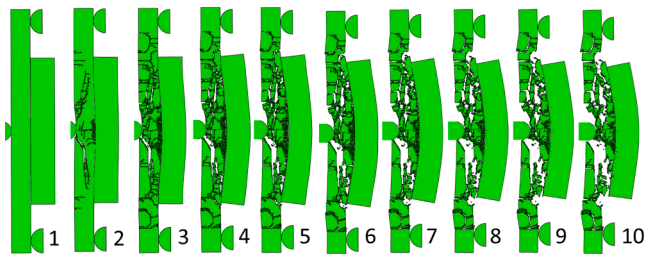


Fig. 39. Comparison between fracture patterns predicted by FEA and experimental results. Impact is at 100 m s^{-1} and the images are spaced by $100 \mu\text{s}$. The backing polymer is Task 11.

series as previously defined in Section 5.2 and the exact parameters are presented in the Appendix. No failure model was implemented in the impact simulation (Table 8).

6.2. Quasi-static FEA response

The results of the quasi-static simulations were compared against experimental results. For Task 3, the room temperature simulations were found to reliably predict the Type 2 failure mode, Fig. 35, producing the double peak behaviour of the beam bend specimens, Fig. 34, but found there was little difference from the addition of the primer pre-treatment. At sub ambient conditions there were more significant differences between the simulated and experimental results because the simulated continued to predict Type 2 (central) failure whilst it was observed that Type 1 (interface) failure occurred. This low temperature discrepancy was likely due to the previously discussed issues of thermally induced strains developing across the interface leading to, experimentally, a weaker interface than in the model. Therefore, the simulation could be used to predict an idealised case at low temperatures where no thermally induced strains are present.

Further, as was previously discussed in this paper, experimentally, the difference between Type 1 (interfacial) failure and Type 2 (central) failure can be influenced by relatively small changes in polymer stiffness and interfacial properties. Therefore, because this simulation has been shown to reliably capture specimen response, it provides an opportunity to investigate the thresholds of the failure modes observed, although such a study would be beyond the scope of this research.

For Task 11, the model captured the failure load well where there was no major double peak behaviour at ambient temperatures, Fig. 36, and this was reflected in the failure mode, Fig. 37. As was observed experimentally, the backing did little to increase the failure stress of the ceramic and then, post ceramic failure, remained bonded for a significant duration. Although, in the simulation, the load sustained by the polymer post ceramic failure was greater than that sustained experimentally. This was thought to be due to local interfacial failure around the centre of the interface, which was not captured in the simulation. This then allowed the backing to sustain greater load than was experimentally observed. Under sub-ambient loading, the double peak behaviour was present, and this is captured accurately by the simulated result. Under these conditions, the simulation results observed that the breaking stress of the ceramic remained unchanged and, once failed, the trough of the double peak loading matched that observed experimentally and captured the post-failure behaviour of the polymer well.

These results show that the relatively simple materials models are able to capture the observed experimental behaviour reasonably well,

although the limitations of these model should be acknowledged. The bilinear approximation of the TSL used, determined from Eq. (5), is a simplification of the response of the interface and would also struggle to capture more ductile behaviour and behaviour under non-monotonic loading. Further, the model was calibrated against data in which failure was primarily in mode 1, and therefore, it was assumed that the shearing component effecting failure was small. Additionally, for the polymers, either perfectly brittle or hyperelastic behaviour was modelled. Whilst this was valid for this research for the temperature and strain rates observed in this study, a more sophisticated model should be adopted for intermediate conditions in which the polymer cannot be approximated as perfectly brittle or hyperelastic.

6.3. Impact FEA comparison

Impact was simulated over the range of impact speeds of interest to this project and the reduction in velocity of the projectile determined, Fig. 38. The simulation reliably predicted the residual speed after impact for each specimen type. Whilst the performance of the different polymer backings was similar, the simulation predicted that the stiffer Task 3 polymer, acting below its glass transition temperature, was able to reduce the speed of the projectile more than Task 11. This is interesting because, despite the Task 11 polymer undergoing an impact induced glass transition which would be highly energy dispersive, the stiffness of Task 3 ultimately allowed for greater energy absorption from the projectile. This implied the overall stiffness of the backing polymer was more influential than any further energy absorptive abilities from the glass transition. Further, the nature of the bonding between the backing polymer and ceramic (fully stuck or strengthless) was found to have only a small influence on the residual velocity of the projectile.

The simulation was found to capture the fracture pathways well under impact when compared to the experimental data, Fig. 39. Discrepancies arose when fracture was observed in the polymer backing because, in this study, the polymer was modelled with a Prony series which could not capture failure. Despite this fundamental difference in observed behaviour, the comparison between the simulation and experiment for Task 3 was no worse than that observed for Task 11 where this fracture-free behaviour was observed. This demonstrated that a significant portion of the incident kinetic energy was transferred to kinetic energy of the fragments, reducing the sensitivity to the mechanical properties of the polymer. Despite this, the interface was experimentally observed to have a degree of influence over the fracture path dynamics and the failure mode of the material, which could be influential for with representative armour materials, plate impact or situations in which the armour has more realistic rear support.

Similarly to the quasi-static model, the material models used in this simulation are relatively simple but are able to capture the overall experimental behaviour well. However, the limits of these models should be considered before these are extended to more complex situation. Firstly, the ceramic uses a rate insensitive elastic-brittle material model which is valid for the impact speeds in this study but will no longer be valid at higher speeds. Further, commutation will occur at greater impact speeds which this model would struggle to capture. Secondly, a simplified interface model was adopted for this study in which the interface was modelled as fully stuck or fully debonded. This is valid for this investigation in which the extremes of interface behaviour was investigated, although more sophisticated models would be needed to explore the interfacial effects in between these two extremes. Finally, a Prony series model was used to capture the polymer response. Whilst this was able to capture the influence of strain rate on the polymer response, it was unable to capture polymer failure. Therefore, this model would struggle to capture experimental behaviour in which the polymer failure was a dominant mechanism.

7. Conclusions

The energy absorptive capabilities of polyurethane-backed alumina specimens loaded under quasi-static and impact three-point bend were investigated using quasi-1D (beam) specimens that allowed fracture paths to be observed that would otherwise have been obscured in typical ballistic impact experiments on plates.

Under quasi-static three-point bend, all specimens failed in one of two failure modes, denoted Type 1 or Type 2. In Type 1, the ceramic-polymer interface began to fail under the applied bending stress before the breaking stress of the ceramics, thus the ceramic was left unsupported and ultimately failed. For Type 2, no interface failure was detected during loading and, after the ceramic ultimately failed, the polymer backing did not and remained bonded to the two halves of the ceramic. In this configuration, the structure was able to continuously withstand substantial load. It was found the difference between Type 1 and 2 failure was dependant upon both the interfacial and polymer properties because it was possible, with the manipulation of temperature, to control the type of failure exhibited. This was important because Type 2 failure presented up to 3x the energy absorption of Type 1. Therefore, the temperature manipulation required could be used to govern the correct polymer for the application because the temperature change required could be used to determine the ideal position of the glass transition temperature and hence predict the most suitable polymer for the task. Further, because FEA simulations were found to reliably predict this response and failure, these provide an opportunity to investigate the threshold between Type 1 and Type 2 behaviour and can be used to predict the polymer properties that would be most suitable for the loading and environmental conditions of the required proposed task.

Under impact, the polymer backing and interfacial properties were found to be influential on performance but the strongest energy absorption mechanism was the kinetic energy of the material fragments. Whilst this mechanism was relatively similar for the specimen types of interest to this project, the quasi-1D nature of this experimental design allowed for these significant differences in fracture path dynamics to be directly observable. These dynamics were observed to be influenced by the behaviour of the interface, so whilst this did not produce significant differences in model armour performance as measured by projectile speeds, it is expected that the effect could be influential for more complex experimental geometries, ballistic impacts on plates, or when loaded in conjunction with ballistic gel backings. FEA simulations calibrated using independently obtained material parameters were used to successfully predict armour behaviour under impact. In these simulations, of the two polyurethanes used the stiffer polymer was found to be superior, despite the second polymer undergoing an impact induced glass transition which would be expected to have been highly energy dispersive.

The principle of time temperature superposition was used by manipulation of the temperature to simulate the impact behaviour of the polymer to link the quasi-static to the dynamic results. However, these results were limited due to the influence of thermally induced strains present over the material boundary, causing premature failure of the interface.

CRedit authorship contribution statement

Tom Commins: Writing – original draft. **Aaron Graham:** Project administration. **Clive R Siviour:** Supervision.

Declaration of Competing Interest

The authors declare that they have no known competing financial interests or personal relationships that could have appeared to influence the work reported in this paper.

Data availability

Data will be made available on request.

Acknowledgements

The authors would like to thank Dstl, in particular to Rebecca Livesey

and Neil Middleton, for their financial and intellectual support during this work under contract number DSTLX1000128371. Additionally, thanks must be extended to Igor Dyson and Nick Hawkins for their experimental and analytical assistance as well as Neil Warland and Andy Bateman for specimen manufacture.

For the purpose of Open Access, the author has applied a CC BY public copyright license to any Author Accepted Manuscript (AAM) version arising from this submission.

Supplementary materials

Supplementary material associated with this article can be found, in the online version, at [doi:10.1016/j.ijimpeng.2023.104708](https://doi.org/10.1016/j.ijimpeng.2023.104708).

Appendix

DSC Data

Differential scanning calorimetry (DSC) was conducted on fully cured specimens of Task 3 and Task 11. The specimens were approximately 10 mg in weight and were heated from -90 to 120 °C at a rate of 3 °C per minute. The glass transition points were found to be at approximately 15 °C and 50 °C for Task 11 and Task 3 respectively, [Fig. A.1](#)

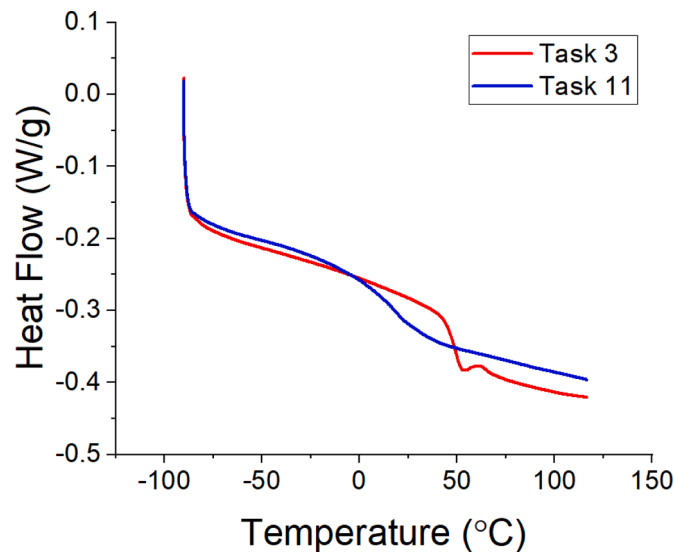


Fig. A.1. DSC results for Task 3 and Task 11.

GFPC DMA data

DMA experiments were conducted on prismatic specimens of glass-fibre reinforced polycarbonate of dimensions 17.5 x 12.1 x 3.5 mm. Specimens were tested in a dual cantilever configuration from -60 to 120 °C in 2 °C increments. An oscillatory testing procedure was implemented and specimens were loaded to an amplitude of 0.1% strain at frequencies of 0.1, 0.316, 1, 3.16, 10 Hz. The principle of time-temperature superposition was used to create the mastercurve presented in [Fig. B.1](#) using the shift factors in [Fig. B.2](#).

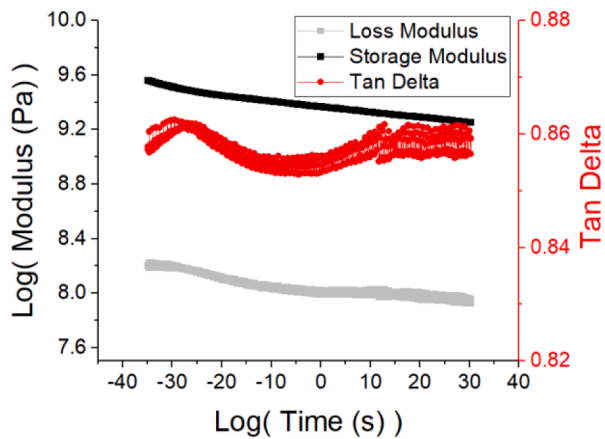


Fig. B.1. Mastercurve of GFPC created using oscillatory single cantilever DMA.

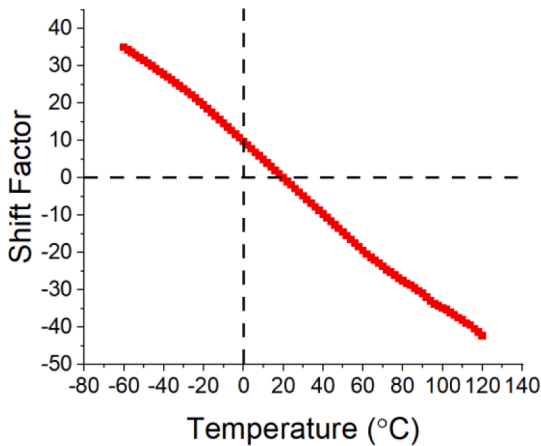


Fig. B.2. Shift factors used to generate the mastercurve for GFPC.

DIC parameters

Table C.1

Table C.1	
Camera properties and DIC processing settings.	
	Point Grey GS3-U3-41C6M-C
Camera Noise	0.9%
Frame Rate	25 fps
Exposure Time	0.02 s
Field of View	2048 x 1200
DIC Software	MatchID.2021.2
Spatial Resolution	0.02 pixels
Subset Size	17 pixels
Step Size	5 pixels
Pixel Size	0.017 mm
Correlation Method	ZNSSD
Image Prefilter	Gaussian, Kernel 5
Interpolation	Bicubic Spline
Shape Function	Quadratic

Task 3 and Task 11 Prony series parameters

Density = 1120 kg/m³

Poissons ratio = 0.49

Ceramic Weibull Modulus

The variation in strength of the unbacked ceramic was initially measured by loading six specimens quasi-statically in three-point bend to produce the force displacement relationships in Fig. E.1. To account for variations in specimen size, the force was then normalised with respect to the second moment of area and modulus of the ceramic; the results are shown to collapse on the same loading line, Fig. E.2.

The breaking stress in the ceramic was calculated for each specimen using the simple beam bend relation

$$\sigma = \frac{M y_{max}}{I} \quad (7)$$

Where M was the bending moment at the centre of the beam, y_{max} is the maximum distance from the neutral axis (i.e. the depth of the beam) and I is the second moment of area. A Weibull distribution was fitted to these results [27], by calculating the probability of failure, P_f , for each specimen and plotting against strength, Fig. E.3. The Weibull modulus was determined to be 17.1, which is high for a ceramic and demonstrates this material has a relatively reliable breaking stress.

Table D.1

Prony series values for Task 3 and Task 11 at 20 °C.

Task 3			Task 11		
E_0	6.34×10^9 (Pa)	(instantaneous)	E_0	4.06×10^9 (Pa)	(instantaneous)
$\log(\tau \text{ (s)})$	g_i	k_i	$\log(\tau \text{ (s)})$	g_i	k_i
-14	0.027024	0.027024	-14	0.099517	0.099517
-13	0.069250	0.069250	-13	0.018718	0.018718
-12	0.120835	0.120835	-12	0.062411	0.062411
-11	0.125524	0.125524	-11	0.023109	0.023109
-10	0.047087	0.047087	-10	0.049524	0.049524
-9	0.031334	0.031334	-9	0.03617	0.03617
-8	0.021768	0.021768	-8	0.034692	0.034692
-7	0.023346	0.023346	-7	0.049993	0.049993
-6	0.024357	0.024357	-6	0.055586	0.055586
-5	0.015738	0.015738	-5	0.064899	0.064899
-4	0.019053	0.019053	-4	0.075297	0.075297
-3	0.018074	0.018074	-3	0.083994	0.083994
-2	0.018484	0.018484	-2	0.092791	0.092791
-1	0.017316	0.017316	-1	0.09826	0.09826
0	0.027450	0.027450	0	0.077958	0.077958
1	0.021815	0.021815	1	0.051643	0.051643
2	0.018705	0.018705	2	0.015981	0.015981
3	0.023883	0.023883	3	0.004859	0.004859
4	0.026377	0.026377	4	0.001534	0.001534
5	0.032628	0.032628	5	0.000939	0.000939
6	0.050860	0.050860	6	2.56E-05	2.56E-05
7	0.069407	0.069407	7	0.000113	0.000113
8	0.082257	0.082257	8	3.27E-06	3.27E-06
9	0.048129	0.048129	9	1.48E-06	1.48E-06
10	0.011567	0.011567	10	1.2E-05	1.2E-05
11	0.002510	0.002510	11	3.15E-05	3.15E-05
			12	0.000527	0.000527
			13	7.43E-12	7.43E-12
			14	0.000666	0.000666
			15	0.000337	0.000337

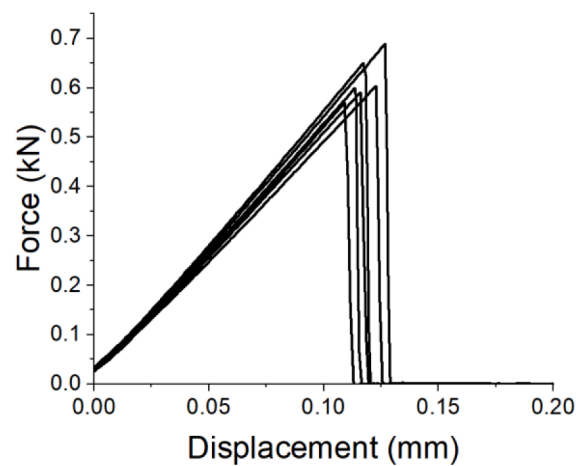


Fig. E.1. Force vs. displacement for unbacked ceramic.

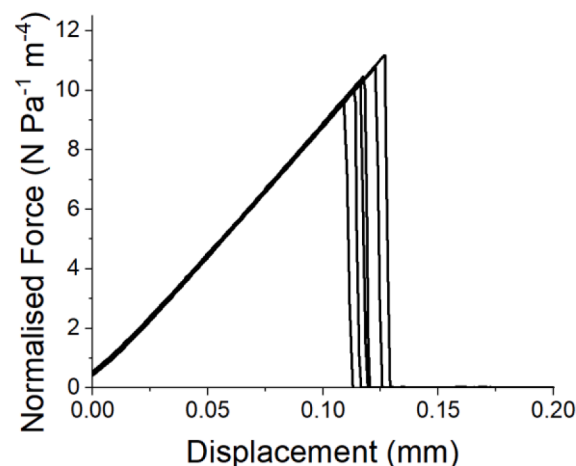


Fig. E.2. Force vs. displacement for unbacked ceramic normalised by Young's Modulus and second moment of area of each specimen to account for geometric effects.

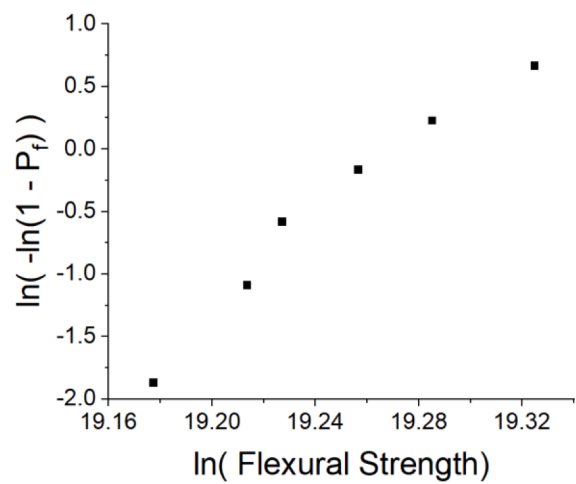


Fig. E.3. Weibull plot for unbacked ceramic loaded under three-point bend.

References

- [1] Crouch IG. Body armour – new materials, new systems. *Defence Technol* Jun. 01, 2019;15(3):241–53. <https://doi.org/10.1016/j.dt.2019.02.002>. China Ordnance Society.
- [2] David Nv, Gao XL, Zheng JQ. Ballistic resistant body armor: contemporary and prospective materials and related protection mechanisms. *Appl Mech Rev Sep*. 2009;62(5):1–20. <https://doi.org/10.1115/1.3124644>.
- [3] Akella K, Naik NK. Composite armour—A review. *J Indian Inst Sci* 2015;95(3): 297–312.
- [4] Hazell PJ. *Armour: materials, theory, and design*. CRC press; 2022.
- [5] Seifert W, Strassburger E, Grefen S, Schaare S. Experimental study about the influence of adhesive stiffness to the bonding strengths of adhesives for ceramic/metal targets. *Defence Technol Apr*. 2016;12(2):188–200. <https://doi.org/10.1016/J.DT.2015.12.002>.
- [6] Zaera R, Sánchez-Sáez S, Pérez-Castellanos JL, Navarro C. Modelling of the adhesive layer in mixed ceramic/metal armours subjected to impact. *Compos Part A Appl Sci Manuf Aug*. 2000;31(8):823–33. [https://doi.org/10.1016/S1359-835X\(00\)00027-0](https://doi.org/10.1016/S1359-835X(00)00027-0).
- [7] López-Puente J, Arias A, Zaera R, Navarro C. The effect of the thickness of the adhesive layer on the ballistic limit of ceramic/metal armours. An experimental and numerical study. *Int J Impact Eng Dec*. 2005;32(1–4):321–36. <https://doi.org/10.1016/J.IJIMPENG.2005.07.014>.
- [8] Prakash A, Rajasankar J, Anandavalli N, Verma M, Iyer NR. Influence of adhesive thickness on high velocity impact performance of ceramic/metal composite targets. *Int J Adhes Adhes Mar*. 2013;41:186–97. <https://doi.org/10.1016/J.IJADHADH.2012.11.008>.
- [9] Übeyli M, Yıldırım RO, Ögel B. Investigation on the ballistic behavior of Al₂O₃/Al₂O₄ laminated composites. *J Mater Process Technol Jan*. 2008;196(1–3): 356–64. <https://doi.org/10.1016/J.JMATPROTEC.2007.05.050>.
- [10] Harris A, Vaughan B, Yeomans J, Smith P, Burnage S. Ballistic testing of surface-treated alumina and silicon carbide with improved adhesive bond strength. *Int J Appl Ceram Technol May* 2017;14(3):323–30. <https://doi.org/10.1111/ijac.12668>.
- [11] Harris AJ, Vaughan B, Yeomans JA, Smith PA, Burnage ST. Surface preparation of silicon carbide for improved adhesive bond strength in armour applications. *J Eur Ceram Soc Dec*. 2013;33(15–16):2925–34. <https://doi.org/10.1016/j.jeurceramsoc.2013.05.026>.
- [12] Yadav S, Ravichandran G. Penetration resistance of laminated ceramic/polymer structures. *Int J Impact Eng* 2003;28(5):557–74.
- [13] Akella K. Studies for improved damage tolerance of ceramics against ballistic impact using layers. *Procedia Eng* 2017;173:244–50.
- [14] Crouch IG. Critical interfaces in body armour systems. *Defence Technol Dec*. 01, 2021;17(6):1887–94. <https://doi.org/10.1016/j.dt.2020.11.006>. China Ordnance Industry Corporation.
- [15] Roland CM. *Viscoelastic behavior of rubbery materials*. OUP Oxford; 2011.
- [16] Bogoslovov RB, Roland CM, Gamache RM. Impact-induced glass transition in elastomeric coatings. *Appl Phys Lett* 2007;90(22). <https://doi.org/10.1063/1.2745212>.
- [17] Roland CM, Fragiadakis D, Gamache RM. Elastomer-steel laminate armor. *Compos Struct Apr*. 2010;92(5):1059–64. <https://doi.org/10.1016/j.compstruct.2009.09.057>.
- [18] Si P, Liu Y, Yan J, Bai F, Huang F. Ballistic performance of polyurea-reinforced ceramic/metal armor subjected to projectile impact. *Materials (Basel) Jun*. 2022; 15(11). <https://doi.org/10.3390/ma15113918>.
- [19] “Morgan ceramics,” <https://www.morgantechnicalceramics.com/en-gb/>.
- [20] “Bentley advanced materials,” <https://www.benam.co.uk/products/plastic/task>.
- [21] Commins T, Siviour CR. Stress relaxation after low and high-rate deformation of polyurethanes (Submitted). *Proceed Royal Society A: Math Phys Eng Sci* 2023.
- [22] “Ensinger plastics,” <https://www.ensingerplastics.com/en-gb/shapes/products/tecanat-gf30-natural>.
- [23] “MatchID,” <https://www.matchid.eu/>.
- [24] M.L. Williams, R.F. Landel, and J.D. Ferry, “Temperature dependence of relaxation mechanisms the temperature dependence of relaxation mechanisms in amorphous polymers and other glass-forming liquids,” 1955. [Online]. Available: <https://pubs.acs.org/sharingguidelines>.
- [25] Wineman AS, Rajagopal KR. *Mechanical response of polymers*. Cambridge: Cambridge University Press; 2000.
- [26] Deng S, Hou M, Ye L. Temperature-dependent elastic moduli of epoxies measured by DMA and their correlations to mechanical testing data. *Polym Test Sep*. 2007;26 (6):803–13. <https://doi.org/10.1016/j.polymertesting.2007.05.003>.
- [27] Weibull W. A statistical distribution function of wide applicability. *J Appl Mech-Trans ASME* 1951;18(3):293–7.
- [28] Serjouei A, Gour G, Zhang X, Idapalapati S, Tan GEB. On improving ballistic limit of bi-layer ceramic–metal armor. *Int J Impact Eng Jul*. 2017;105:54–67. <https://doi.org/10.1016/j.ijimpeng.2016.09.015>.
- [29] Jonas GH, Zukas JA. Mechanics of penetration: analysis and experiment. *Int J Eng Sci* 1978;16(11):879–903.
- [30] Ben-Dor G, Dubinsky A, Elperin T. On the Lambert–Jonas approximation for ballistic impact. *Mech Res Commun* 2002;29(2):137–9. [https://doi.org/10.1016/S0093-6413\(02\)00246-X](https://doi.org/10.1016/S0093-6413(02)00246-X).
- [31] Commins T, Siviour CR. The use of time-temperature superposition for interface characterisation using the J-integral (Submitted). *Strain* 2023.
- [32] Cherepanov GP. The propagation of cracks in a continuous medium. *J Appl Math Mech* 1967;31(3):503–12.
- [33] J.R. Rice, “A path independent integral and the approximate analysis of strain concentration by notches and cracks,” 1968.
- [34] Sun F, Blackman BRK. A DIC method to determine the Mode I energy release rate G, the J-integral and the traction-separation law simultaneously for adhesive joints. *Eng Fract Mech* 2020;234:107097.
- [35] Anderson TL. *Fracture mechanics: fundamentals and applications*. CRC press; 2017.